Study of Minority Carrier Lifetime and Transport in InAs/InAsSb type-II Superlattices Using a Real-Time Baseline Correction Method

by

Zhiyuan Lin

A Dissertation Presented in Partial Fulfillment
of the Requirements for the Degree
Doctor of Philosophy

Approved November 2016 by the
Graduate Supervisory Committee:

Yong-Hang Zhang
Dragica Vasileska
Shane Johnson
Michael Goryll

ARIZONA STATE UNIVERSITY

December 2016

ABSTRACT

Sb-based type-II superlattices (T2SLs) are potential alternative to HgCdTe for infrared detection due to their low manufacturing cost, good uniformity, high structural stability, and suppressed Auger recombination. The emerging InAs/InAsSb T2SLs have minority carrier lifetimes 1-2 orders of magnitude longer than those of the well-studied InAs/InGaSb T2SLs, and therefore have the potential to achieve photodetectors with higher performance. This work develops a novel method to measure the minority carrier lifetimes in infrared materials, and reports a comprehensive characterization of minority carrier lifetime and transport in InAs/InAsSb T2SLs at temperatures below 77 K.

A real-time baseline correction (RBC) method for minority carrier lifetime measurement is developed by upgrading a conventional boxcar-based time-resolved photoluminescence (TRPL) experimental system that suffers from low signal-to-noise ratio due to strong low frequency noise. The key is to modify the impulse response of the conventional TRPL system, and therefore the system becomes less sensitive to the dominant noise. Using this RBC method, the signal-to-noise ratio is improved by 2 orders of magnitude.

A record long minority carrier lifetime of 12.8 μs is observed in a high-quality mid-wavelength infrared InAs/InAsSb T2SLs at 15 K. It is further discovered that this long lifetime is partially due to strong carrier localization, which is revealed by

temperature-dependent photoluminescence (PL) and TRPL measurements for InAs/InAsSb T2SLs with different period thicknesses. Moreover, the PL and TRPL results suggest that the atomic layer thickness variation is the main origin of carrier localization, which is further confirmed by a calculation using transfer matrix method.

To study the impact of the carrier localization on the device performance of InAs/InAsSb photodetectors, minority hole diffusion lengths are determined by the simulation of external quantum efficiency (EQE). A comparative study shows that carrier localization has negligible effect on the minority hole diffusion length in InAs/InAsSb T2SLs, and the long minority carrier lifetimes enhanced by carrier localization is not beneficial for photodetector operation.

ACKNOWLEDGMENTS

This thesis is completed under the very helpful guidance of my supervisor Professor Yong-Hang Zhang. Professor Zhang's extensive knowledge of physics, meticulous approach of research, rigorous work style, patient way of teaching, and amiable personality deeply influenced and inspired me, and will have profound impacts on me. His guidance not only helped me establish academic goals, obtain the fundamental methodology of conducting scientific research, but also illustrated me with many useful principles of how to communicate with people and how to tackle problems. Here I would like to express my great respect and heartfelt thanks to him.

I must also thank my committee members Professor Dragica Vasileska, Dr. Shane Johnson and Professor Michael Goryll. Their assistance, guidance and support greatly accelerated the progress toward my academic goal and paved solid foundation for the completion of my thesis.

During my research, many colleague students and researchers helped me or involved in the work of this thesis. I would like to thank Zhao-Yu He for device fabrication and proofreading this thesis, Dr. Orkun Oray Cellek for enormous guidance at the beginning of my PhD career, Dr. Xiao-Meng Shen and Dr. Elizabeth Steenbergen for sample characterization and helpful discussion, Dr. Shi Liu and Dr. Hua Li for sample growth, Dr. Martyn Fisher for proofreading my thesis, Dr. Ha-Sul Kim, Xin-Hao Zhao, Yuan Zhao, Dr. Jin Fan, Dr. Jing-Jing Li, and many others that had provided help toward my PhD degree.

Finally, I would like to thank my parents for their consistent support during my PhD study. They are always my truly trustworthy allies who help me to overcome all kinds of difficulties with invincible love.

TABLE OF CONTENTS

Page

CHAPTER Page

LIST OF TABLES

LIST OF FIGURES

Figure Page

Figure Page

Figure Page

1.INTRODUCTION

Infrared photodetection technology is widely used for night vision, surveillance systems, astronomy, chemical identification, art history and restoration, and petroleum exploration, etc. Semiconductor photodetector is a typical infrared photodetector with high sensitivity. HgCdTe has become the most widely used semiconductor material for infrared phototdetectors. By tuning the Hg composition, a very wide infrared spectral range of 1 μm to 30 μm can be achieved. The change of Hg composition leads to extremely small change of the lattice constant, ensuring that the high quality layers and heterostructures can be grown [1]. Also, HgCdTe has well understood band structure, substantially improved material crystalline quality, and the precisely controlled doping profile [1]. However, the minority carrier recombination process in the state-of-the-art HgCdTe is limited by its intrinsic Auger recombination [2], and the small effective mass could lead to high tunneling dark current that limits the detectable wavelength, especially for the long-wavelength infrared regime [3].

1.1. InAs/InAsSb Type-II Superlattices

InAs/InAsSb type-II superlattice (T2SL) is a promising material for infrared applications as an alternative to HgCdTe. Since the first growth by MOCVD [4], InAs/InAsSb T2SL has been successfully demonstrated for mid-infrared lasers [5][6], LEDs [7], and proposed for IR detectors [8]. Recently, InAs/InAsSb T2SL is demonstrated for long-wave infrared nBn photodetectors [9].

Like other Sb-based T2SLs, InAs/InAsSb T2SLs has many advantages over HgCdTe. Two key features include the suppressed Auger recombination and large effective mass. The dominant Auger process in the state-of-the-art HgCdTe materials are Auger 1, which involves two electrons and one heavy hole, and Auger 7, which involves one electron, one heavy hole and one light hole. In superlattices, the width of the electron minibands can be engineered to be narrower than the effective band gap, limiting the available final states of the electrons and eliminates the Auger 1 transition for momentum in the superlattice direction. Also, due to both strain and quantization effects, the splitting between heavy and light hole is larger than the effective band gap, reducing the Auger 7 transition probability [3][10]. Due to the band structure, the effective masses are relatively large along the superlattice direction compared with bulk HgCdTe, leading to a low band-to-band tunneling current [3][11][12]. In addition, a schematic band edge diagram of a T2SL is shown in Figure 1.1. The interband optical transition in the T2SL is spatially indirect. Therefore, the smallest effective band gap is not limited by the constituent materials [5]. They also have more uniform material in the wafer due to good control of alloy composition, and have stronger bonds and structural stability, which may lead to a better device yield, reliability and radiation tolerance [13].

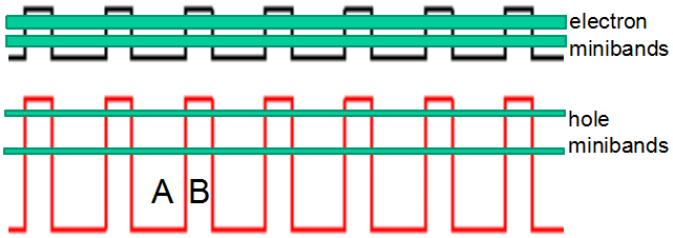

Figure 1.1. Band edge alignment in a type-II superlattice composites with materials A and B.

In the InAs/InAsSb T2SL, the absence of Ga simplifies the T2SL interface and material growth as compared with the traditional InAs/InGaSb T2SL [6][14]. Some early work prefers InAs/InGaSb strained layer T2SL over InAs/InAsSb T2SL for the same operation wavelength because InAs and InGaSb has a broken gap band alignment, thus the InAs/InGaSb T2SL requires thinner periods to reach the same cut-off wavelength, leading to a larger electron and hole wave function overlap and thus larger absorption coefficients [15]. A theoretical study suggests an absorption coefficient of 2000 cm^{-1} for a LWIR InAs/$In_{0.4}Ga_{0.6}Sb$ T2SL and an absorption coefficient of 1500 cm^{-1} for a LWIR InAs/$InAs_{0.61}Sb_{0.39}$ T2SL with a similar cut-off wavelength, and the performance of the ideal InAs/$In_{0.4}Ga_{0.6}Sb$ T2SL device is only slightly better than the ideal InAs/InAsSb T2SL device [16]. Therefore, the device performance of the InAs/InAsSb and InAs/InGaSb T2SL photodetectors may be dominantly determined by other non-intrinsic material properties rather than the absorption coefficients, such as Shockley-Real Hall (SRH) mechanisms [16].

Minority carrier lifetime is a key material property that determines the dark

current and carrier extraction performance of photodetectors. The minority carrier lifetime of InAs/InGaSb T2SL is only near 30 ns, dominated by SRH recombination [17][18][19]. On the other hand, longer minority carrier lifetimes of 412 ns at 77 K in a long-wavelength infrared InAs/InAsSb T2SL is experimentally observed [20], which is one order of magnitude longer than that of the InAs/InGaSb T2SLs. In the mid-wavelength infrared regime, minority carrier lifetimes as long as 9 μs [21], 10 μs [22], and 12.8 μs [23] was reported, 2 orders of magnitude longer than those of InAs/InGaSb T2SLs. Lower SRH recombination rates in InAs/InAsSb T2SLs is the key reason for these longer minority carrier lifetimes.

Further investigations indicate that there could be an intrinsic mid gap defect level acting as SRH recombination center in the InAs/InGaSb T2SLs [24], making the short SRH recombination lifetime an intrinsic material property. By contrast, the InAs/InAsSb T2SLs have lower band edges, and the mid-gap SRH recombination center can potentially locate inside the conduction band, not contributing to the minority carrier recombination processes. This hypothesis is confirmed by pressure dependent photoluminescence (PL) measurements, which reveal that a trap state 0.18 eV above the conduction band edge of a mid-wavelength infrared InAs/InAsSb T2SL [25]. Therefore, it is easier to achieve a long minority carrier lifetime due to low SRH recombination rate in InAs/InAsSb T2SLs compared with InAs/InGaSb T2SLs, indicating reduced dark current and improved quantum efficiency in the devices.

Recent material optimization has greatly suppressed the SRH recombination rates, and leads to radiative recombination limited minority carrier lifetimes in the mid-wavelength infrared InAs/InAsSb T2SLs of a few microseconds [26][27]. With the minority carrier lifetime dominated by the radiative recombination, a reduction of background carrier concentration is suggested to further improve the minority carrier lifetime for a suppressed photodetector dark current [28].

1.2. Minority Carrier Lifetime Measurement

Even though the long minority carrier lifetimes have been observed in InAs/InAsSb T2SLs, some of the mechanisms that leads to long minority carrier lifetimes are not fully understood yet. It is therefore necessary to investigate the minority carrier lifetimes at cryogenic temperatures which reveal abundant information of carrier recombination processes. Multiple methods are reported to determine the minority carrier lifetimes in the T2SLs, including time domain methods time-resolved pump and probe for differential transmission measurement [21], time-resolved photoluminescence (TRPL) measurement [17], and frequency domain method optical modulation response method [18]. Among them, TRPL experiment has a relatively simple configuration as compared with the other time-domain methods, and more straightforward than the frequency domain methods.

However, it is challenging to measure the TRPL because the TRPL measurements of narrow bandgap materials in the infrared waveband usually has a low

signal-to-noise ratio due to several reasons. First, the material properties under low excess carrier density conditions are particularly valuable since many photodetectors operate in the low-injection regime, but low excess carrier density brings low PL intensities. Second, compared with the materials working in the visible waveband, the materials working in the infrared waveband give relatively weak PL intensity due to their low radiative-recombination coefficients, as compared to the large non-radiative recombination coefficients in these materials. Third, ambient radiation causes strong background noise in the infrared regime. Additionally, photodetectors used for collecting the infrared light have limited performance. The success of the measurement of weak TRPL signals with significant noise in narrow bandgap materials [17] relies on a critical step which digitizes the signal rapidly (~ GHz).

Boxcar technique represents a low-cost alternative for direct time-domain TRPL measurements in infrared waveband. However, unlike the digitizer that can utilize all the photons, the boxcar utilizes only the photons within a small time window, so the conventional boxcar technique suffers from strong baseline noise and weak noise suppression capabilities in TRPL measurements. The desired PL signal is usually buried in the noise under low excitation conditions. Therefore, a major upgrade is desired for the boxcar technique to improve the signal-to-noise ratio for TRPL measurements.

1.3. Organization of the Dissertation

In this thesis, a novel method is invented to upgrade the conventional boxcar-

based TRPL measurement system for the minority carrier lifetime characterization of infrared materials. Using this method, a record long carrier lifetime is demonstrated as 12.8 μs at 15 K, and it is revealed that the long lifetime is partially due to carrier localization. Furthermore, the impacts of carrier localization on the minority carrier diffusion lengths is investigated.

Chapter 2 describes a novel method that can significantly improve the signal-to-noise ratio of the boxcar-based TRPL experiment. This new method is called "real-time baseline correction method" (RBC method). In section 2.1, the experimental apparatus of the conventional TRPL experimental method is described. Section 2.2 analyzes the noise issue in the experimental system. The 1/f noise and baseline fluctuation noise are dominant. Section 2.3 described the modification of the conventional method using the novel RBC method, and the fundamental idea of how the noise suppression is achieved. Further analysis is made in section 2.4 about the noise suppressing mechanism and the system operation, the noise suppressing mechanism is summarized as a notch filter that can effectively eliminate the noise at frequencies other than the modulation frequency. In section 2.5, a simulation of measurement procedures of the two methods confirms that the RBC method is more capable of suppressing the low frequency noises. Section 2.6 provides a comparison between the performance of the two systems is made, and it shows that the signal-to-noise ratio is improved by 2 orders of magnitude using the RBC method. Some practical

issues are discussed in Section 2.7. Section 2.8 is a summary of Chapter 2.

Chapter 3 described the study of minority carrier lifetimes which leads to the discovery of carrier localization, using PL and TRPL experiments in InAs/InAsSb T2SLs. Section 3.1 introduces carrier localization in semiconductors. Section 3.2 provides experimental evidences of carrier localization in InAs/InAsSb T2SLs. A long minority carrier lifetime of 12.8 μs is demonstrated in Sample B at 15 K. The PL peak blue shift from 15 K to 50 K in Sample B along with the line width broadening demonstrates the carrier localization in Sample B. On the other hand, Sample C does not show carrier localization. The carrier localization is attributed to the layer thickness fluctuation of one atomic layer. Section 3.3 demonstrate a calculation of electron and hole energy shift under layer thickness disorder, and demonstrate that the layer thickness fluctuation is the origin of carrier localization in these InAs/InAsSb T2SLs at 15 K. Some possible influence of carrier localization on photodetector performance is discussed in Section 3.4. This chapter is summarized in Section 3.5.

While Chapter 3 discovers carrier localization in InAs/InAsSb T2SLs, Chapter 4 further studies the influence on the vertical minority carrier diffusion length of photodetectors. Section 4.1 describes several methods for vertical minority carrier diffusion length determination. The simulation of external quantum efficiency (EQE) spectra are used for the vertical transport characterization in this chapter, and the details of this method is described in Section 4.2. The EQE spectra and absorption coefficients

of two samples made of InAs/InAsSb T2SLs with PIN structure are measured and discussed in Section 4.3. Section 4.4 discusses the fitting of experimental data using the model. In Section 4.5, carrier localization is identified in one of the samples below 40 K using optical approaches described in Chapter 3. In Section 4.6, the temperature dependence of minority carrier diffusion length is discussed and demonstrates that carrier localization does not influence the minority carrier diffusion length. Section 4.7 summarizes this chapter.

2. A REAL-TIME BASELINE CORRECTION METHOD FOR TIME-RESOLVED INFRARED PHOTOLUMINESCENCE

Time-resolved photoluminescence (TRPL) is broadly-used to characterize the carrier dynamics in bulk materials and hetero-interfaces. The TRPL experiment measures the photoluminescence (PL) decay after a short laser pulse. For wide bandgap materials, the single photon counting technique provides sufficient signal-to-noise ratio to recover the PL decay. For narrow bandgap materials in the infrared waveband, however, it is difficult to measure the TRPL due to its low signal-to-noise ratio in nature. First, the material properties under low excess carrier density conditions are particularly valuable since many photodetectors operate in the low-injection regime, but low excess carrier density brings low PL intensities. Second, compared with the materials working in the visible waveband, the materials working in the infrared waveband give relatively weak PL intensity due to their low radiative-recombination coefficients, as compared to the large non-radiative recombination coefficients in these materials. Third, ambient radiation causes strong background noise in the infrared regime. Additionally, photodetectors used for collecting the infrared light have limited performance.

There have recently been reports on the measurement of weak TRPL signals with significant noise in narrow bandgap materials [17]0. The approaches used in these reports include a critical step which digitizes the signal rapidly (~ GHz). The boxcar technique is a lower cost alternative for direct time-domain TRPL measurements in the

infrared waveband. However, unlike the digitizer that can utilize all the photons, the boxcar utilizes only the photons within a small time window, so the conventional boxcar technique suffers from strong baseline noise and weak noise suppression capabilities in TRPL measurements. The desired PL signal is usually buried in the noise under low excitation conditions. This chapter describes a real-time baseline correction (RBC) method that adds cost-effective equipment to the conventional boxcar-based TRPL system. This method significantly enhances the signal-to-noise ratio by suppressing the noise, and therefore makes it easy to resolve the TRPL signal.

2.1. Boxcar Operation Principle and the Conventional Boxcar-Based Method

At the heart of this method for TRPL measurement is a boxcar averager. A boxcar averager is a sampling instrument which integrates the input signal during a predefined gate width, after a delay following an applied trigger. When the input signal is periodic, the boxcar averager can recover waveforms by sweeping between the initial delay and final delay. The gate width is much shorter than the signal period. The boxcar averager typically takes a set of n samples at certain delay and calculates their average to reduce high frequency noise. The signal waveform recovering process is illustrated schematically in Figure 2.1. The first set of samples is taken after the initial delay. After being averaged by the output averager, the signal intensity value appears as point A on the output plot. After the signal value at this initial delay is measured, the delay is increased by a fixed amount, and the cycle repeats, resulting in point B. As the process

continues, point C and further points are generated, and the delay eventually reaches the preset final delay value. As the process completes, the waveform is replicated as the output. In this case the boxcar can be regarded as a time translation device that can slow down and recover fast waveforms. Unlike some common sampling techniques which take a snapshot of the signal level at one point of time, the boxcar technique takes an average of the signal over the time window, and thus some high frequency noise can be removed.

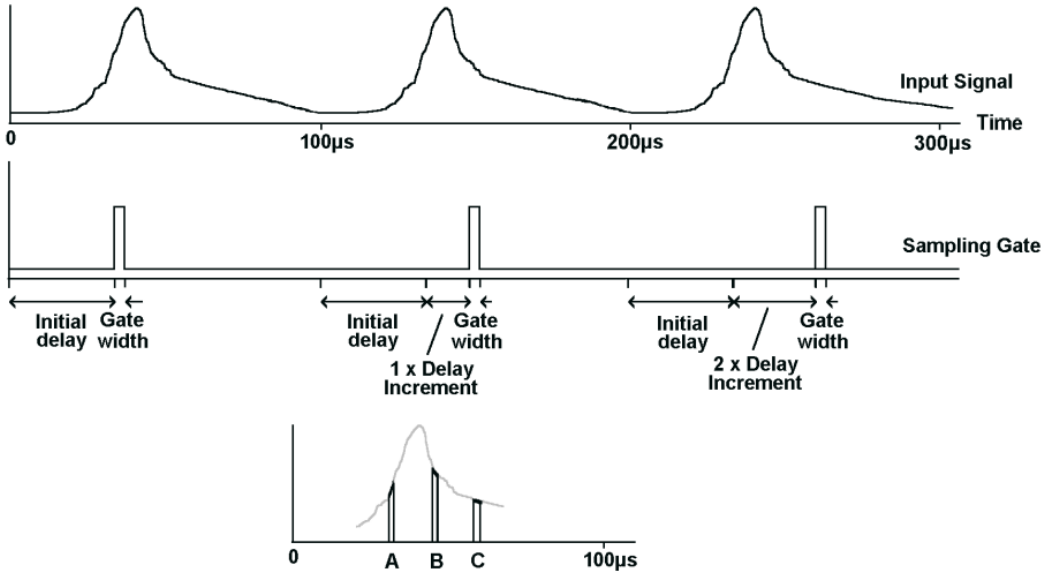

Figure 2.1. Boxcar working principle, taken from reference [29]0.

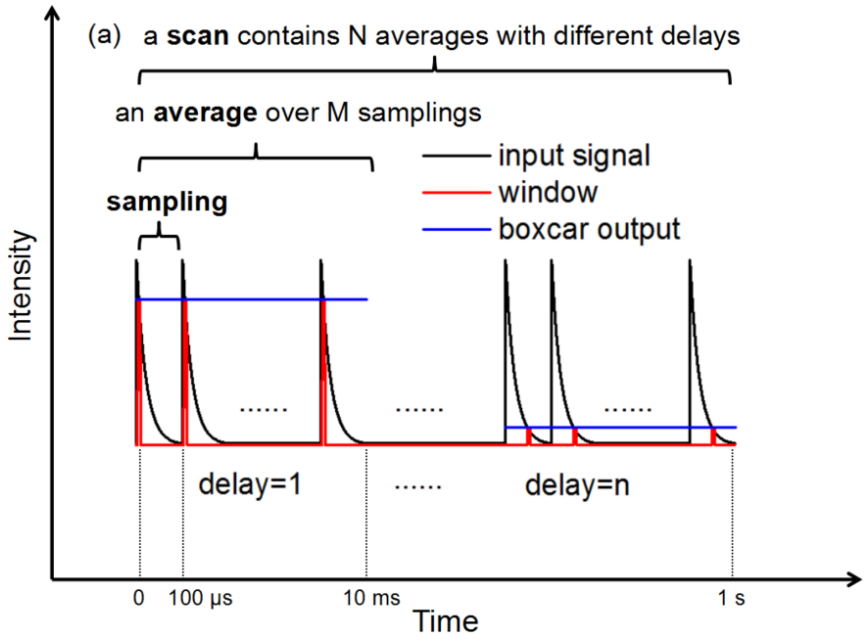

Figure 2.2. Definition of a sampling, an average and a scan during a boxcar-based measurement.

Table 2.1. Definitions of Concepts in the Conventional Method. M Is Number of Sampling, and N is the Number of Delays in Each Scan.

Concept	**Definition**	**Period**
Sampling	Taking a value from one boxcar sampling	t_0
Average	Averaging over outputs of continuous M samplings with the same boxcar delay	$M \times t_0$
Scan	Measuring a curve consisting of averages with delays sweeping over the desired range	$N \times M \times t_0$

Some concepts used in the following text are defined and illustrated in Figure

2.2 and Table 2.1. In each period, the boxcar takes one value of the signal at a certain delay, this step is referred to as a “sampling” process. At each delay, the boxcar takes multiple samplings and calculates the average value, filtering out the sampling to sampling statistical fluctuations, this process is referred to as an “average” process. Finally, multiple averages are taken, and the delay is swept from the initial to the final delay. This process is referred to as the “scan” process. These concepts are used throughout this chapter.

A schematic block diagram in Figure 2.3 shows an example of a TRPL system which utilizes the conventional boxcar technique (this method is referred to as “conventional method” in this chapter). In this system, the sample is mounted inside a cryostat. The sample is excited using a pulse laser having a central wavelength of 1064 nm, a pulse width of 0.5 ns, and a repetition rate of 10 kHz. The PL is directed by 4 gold parabolic mirrors into a high-speed liquid-nitrogen cooled HgCdTe detector with a cutoff wavelength of 11.5 μm and a time resolution of 20 ns. A 3-12 μm band pass filter is placed in front of the detector to filter out any scattered laser light, to avoid damage of the detector due to strong laser light, and also to make the photocurrent of the detector proportional to the PL intensity from the sample as a function of time. The detector current is amplified by a transimpedance preamplifier, and then the amplified signal enters the boxcar averager which is synchronized with the pulse laser. A computer controls the boxcar delay and records the boxcar output, so that the PL

intensity as a function of time (TRPL signal) is measured.

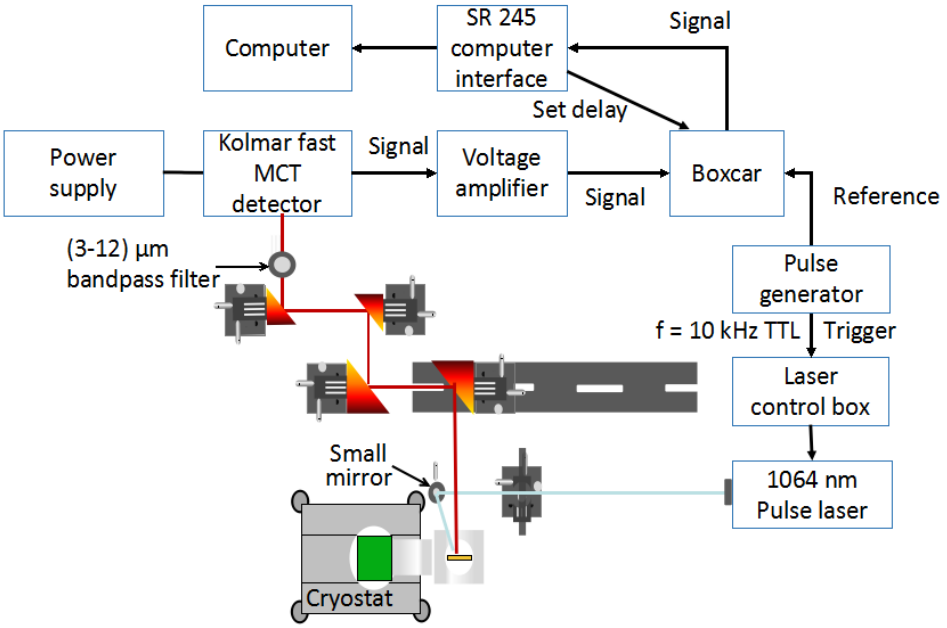

Figure 2.3. The experimental setup of the conventional boxcar-based TRPL experiment.

2.2. Noise in the Conventional Boxcar-Based Method

Infrared detectors work in low excitation regimes with excess carrier density lower than $10^{15}/cm^3$. The initial excess carrier density excited by the laser can be as high as $10^{18}/cm^3$, but only when the decay reaches a small enough excess carrier density ~ $10^{15}/cm^3$ will it give valuable information about the relevant material properties for infrared detectors. Low excess carrier density corresponds to low PL intensity. To resolve this part of the PL decay, it requires a significantly lower noise than the weak PL signal so that the PL signal can be distinguished.

The main noise in the conventional boxcar-based method consists of two parts. First, the 1/f noise is identified to be dominant from 10 Hz to 3 kHz in this experiment.

A lock-in amplifier is used to measure the noise power spectrum by manually sweeping the frequency. The measured noise spectrum of a single output (i.e. one average contains only one sampling) from the boxcar in Figure 2.4 shows that the total noise is dominated by the 1/f noise from 10 Hz to 3 kHz. The equipment is incapable of resolving noise below 0.5 $(\mu V)^2/Hz$. The 1/f noise is tested and confirmed to be independent of the boxcar delay. This noise includes the noise from the detector, the amplifier, the boxcar, the laser and the cables. By measuring the noise at different points along the signal path, it demonstrates that this 1/f noise mainly comes from the detector. The white noise that typically appears in the high frequency domain, such as Johnson noise and shot noise, is beyond the measurement sensitivity in this experiment.

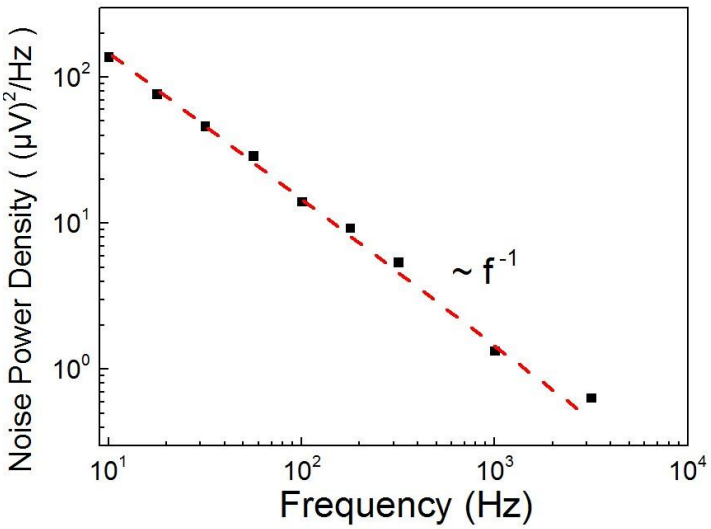

Figure 2.4. The measured noise spectrum in the TRPL experiment from a single boxcar output.

The second part of the noises is a strong sub-Hertz noise associated with the boxcar baseline fluctuation. The boxcar output is the sum of the TRPL signal and the baseline (this total output is referred to as the "received signal" in this chapter). The baseline of the boxcar is a function of delay, and it differs depending on the experimental conditions. In this experiment, the baseline has a strong oscillation following the laser pulse, as shown in Figure 2.5.

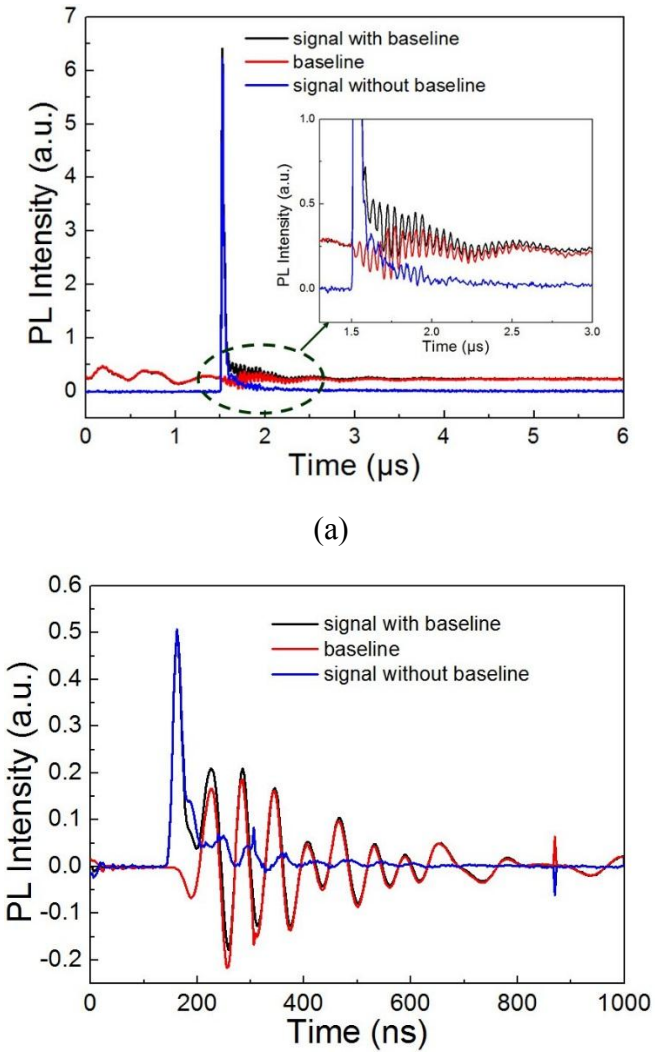

Figure 2.5. Boxcar baseline fluctuation issue. The baseline fluctuation cannot be fully

canceled by subtracting the measured baseline (red) from the measured signal (black). The curves after subtraction are shown in blue. The strong PL signal in (a) keeps a recognizable shape, but the weak PL signal in (b) is buried in the baseline noise.

A few things are done in order to identify where the oscillation is from. It is discovered that when the laser is off, the oscillations disappear. A further test shows that the signal can be detected using an antenna connecting to an oscilloscope when the laser is on, this shows the laser emits a parasitic electromagnetic wave around it when it is operating. By placing the laser far away from the other electronics including the boxcar and the detector, the intensity of the baseline oscillation can be reduced. However, even if the laser is placed in a Faraday cage to block the parasitic electromagnetic wave, the oscillation is not completely removed. Two experiments were performed next. First, an opto-electro coupler is inserted between the laser trigger channel and the pulse generator which triggers the laser. However, this does not change the oscillation at all, which proves that the oscillations do not relate with the trigger. Second, an uninterrupted power supply (UPS) is used as the laser power source to prevent any interaction between the laser and the wall-plug power line, and the baseline oscillation intensity is reduced. It is therefore concluded that the baseline is generated by both the parasitic electromagnetic wave coming from the laser and the coupling from the wall-plug electricity with the laser power source. By screening these two sources, the oscillation is completely removed, however, the experimental system becomes too

bulky to allow handling flexibility in narrow space. Therefore, it is desired to have an alternative method to remove the baseline oscillations.

To resolve the TRPL signal, the baseline needs to be measured and subtracted from the received signal in the TRPL experiment. Since the laser contributes to the baseline, it has to be kept on while collecting the baseline to ensure a correct baseline subtraction. For this reason, in the conventional method, the received signal is collected with the laser beam illuminating the sample, and the baseline has to be collected separately with the laser beam blocked. Figure 2.5(a) shows the experimentally received signal and baseline of the conventional method. An important assumption of the conventional method is that the baseline does not change from measurement to measurement. However, the laser block/unblock frequency is on the order of (0.1 ~ 1) Hz, and the baseline will have changed when switching between the signal measurement and the baseline measurement in such time scale. Therefore, simply subtracting the baseline cannot fully cancel it, as can be seen in Figure 2.5(a), the subtracted signal (blue curve) has strong residuals of the baseline because the parasitic electromagnetic wave significantly contributes to the baseline and introduces significant noise. The strong PL signal in Figure 2.5(a) still suffer from the baseline variation. On the other hand, a weaker PL signal, as seen in Figure 2.5(b), is almost buried in the baseline fluctuation residuals. The baseline oscillation comes after the excitation by the laser pulse, lasting from 200 ns to 1000 ns. Such drift can be attributed

to the fluctuations in and around the experimental system [30]. This noise is referred to as “baseline noise” in the following text.

To suppress the baseline noise, a straightforward way is to screen the laser interference. The laser has to be placed inside a Faraday cage and also it has to be powered by an UPS. However, these shielding components significantly increases the volume of the experimental equipment, making it more difficult to arrange the experiment in a small space and do the optical alignment. A new method for baseline noise suppression is therefore desired to avoid the inconvenience. It will be demonstrated later that this new method also has the advantage that the low frequency noise components can be suppressed without identifying the sources, making it adaptable to more complex situations.

2.3. Real-Time Baseline Correction Method

The noise in this experimental system is dominated by 1/f noise and baseline noise, both of which are significant at low frequencies. This is very similar to the conventional Fourier-transform infrared spectroscopy (FTIR) system. In the conventional FTIR experiment, since the signal is measured on top of the background blackbody spectrum, the ambient temperature fluctuation leads to a significant change of the signal intensity. Therefore, the measured results usually contain strong background noise. Thus, a “double-modulation” method was proposed, and is now widely used for the FTIR technique, to suppress the low frequency temperature

fluctuation problem [31]. In this “double-modulation” method, the signal is modulated at a frequency much higher than the interferogram frequency, and the fluctuation noise is suppressed “frame by frame”. Here the author develops the RBC method to suppress the low frequency noise in the boxcar-based TRPL system, by “double modulating” the laser.

As the “double-modulation” method does in the FTIR experiment, the RBC method also introduces a signal modulation into the experimental procedure. Unlike the “double-modulation method”, which modulates the signal at a very high frequency, the RBC method modulates the signal with a much lower frequency than the pulse frequency of the laser. The double-modulation method and the RBC method are compared in Table 2.2.

Table 2.2. Comparison between the Double Modulation Method and the RBC Method

Method	**Application**	**Purpose**	**Additional modulation frequency**
Double-modulation	FTIR	Suppress low frequency noise	High
RBC	TRPL	Suppress low frequency noise	Low

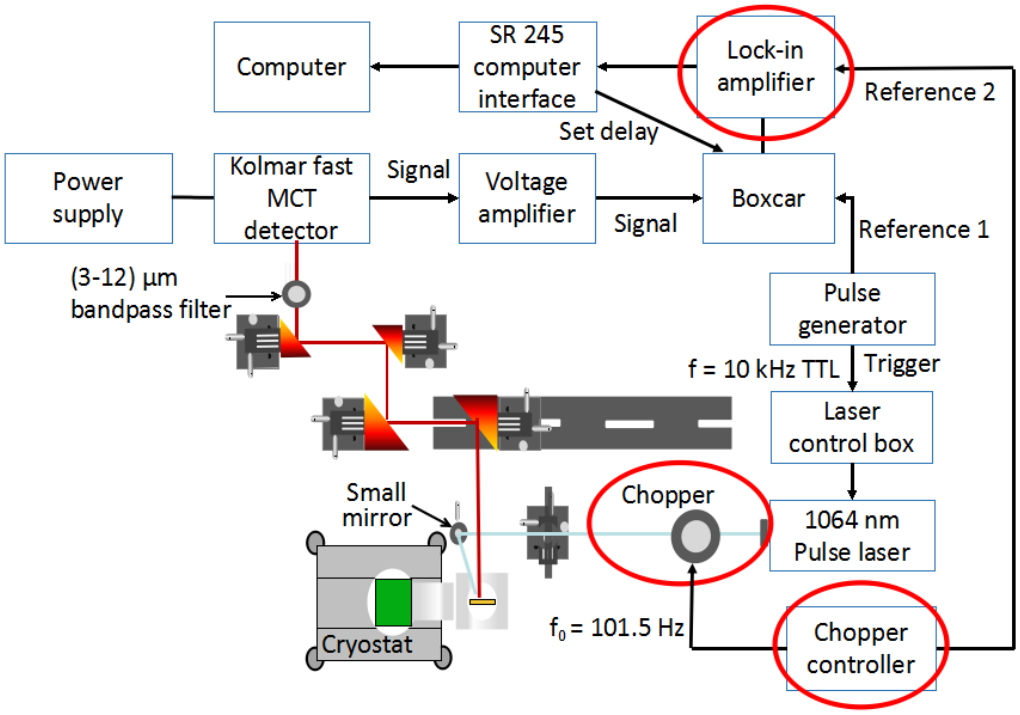

Figure 2.6. The experimental setup of the boxcar-based TRPL experiment using RBC method.

The modified TRPL experimental system using the RBC method is shown in Figure 2.6. A chopper is placed in front of the laser to modulate the laser beam mechanically at a frequency of 100 Hz to 800 Hz, much lower than the frequency of the laser pulse rate of 10 kHz. By doing this, the boxcar output alternates between "received signal" and "baseline" at the frequency of the chopper. The width of the chopper blade is 100 times larger than the laser beam diameter, ensuring that the partial blocking of the laser beam occurs during only 2 % of the total time in each cycle. With this mechanical modulation for the light beam with the laser kept on, the real baseline due to the laser is subtracted more precisely than the conventional method (as

previously stated, the laser contributes to the baseline). A lock-in amplifier synchronized with the chopper is inserted between the boxcar averager and the computer to measure the difference between the received signal and the baseline. The time constant of the lock-in amplifier is set to 3 times the modulation period of the chopper.

Figure 2.7 shows how the modulation of the chopper influences the signal output from the detector. In the conventional method, the system takes multiple samplings for the same delay (Figure 2.7(a)), and then gives the average value (Figure 2.7(b)). Multiple of this average with different delay consist a scan of signals, and then a separate scan for the baseline. In the RBC method, the chopper modulates the laser so that the signal with the same delay is divided into a few “on” and “off” states. As a result, the system alternatively takes a sampling of the signal and baseline, repeatedly (Figure 2.7(c)), and then calculates their average values respectively (Figure 2.7(d)). In the square wave of Figure 2.7(d), the high level corresponds to the received signal value at the delay, and the low level corresponds to the baseline value. The difference between the high and low levels are then measured by a lock-in amplifier. With the modulation, the RBC method switches between received signal and baseline measurements at much higher frequency than the conventional method.

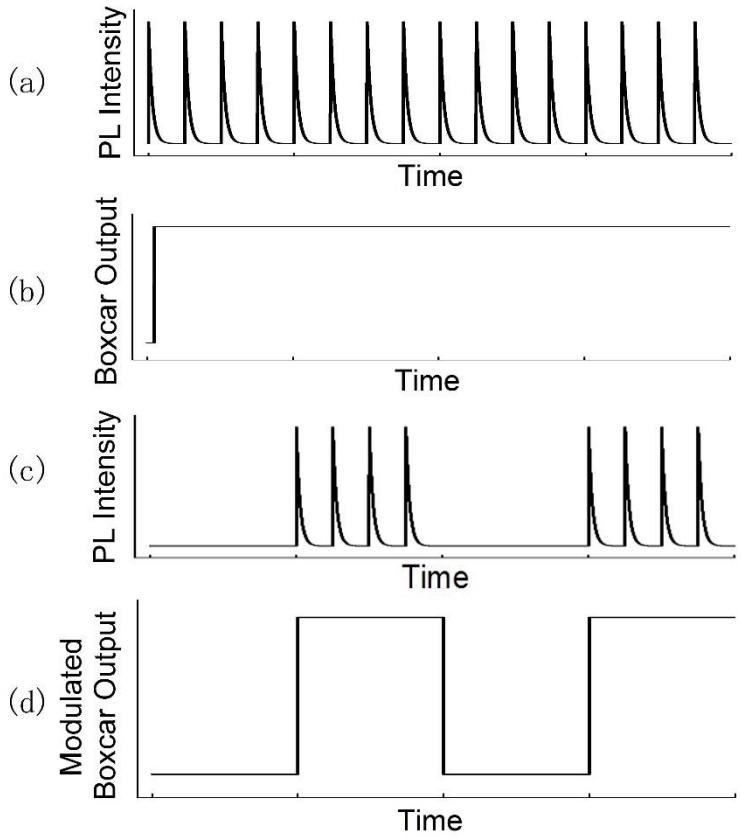

Figure 2.7. Modification of the boxcar output signal in the RBC method. (a) is the voltage coming out from detector without modulation. The boxcar has a fixed delay and measured output (b). The voltage coming out from the detector becomes (c) after modulation, leads to the final boxcar output (d).

Figure 2.8 schematically compares the TRPL measurement procedures using the conventional method and the RBC method. The received signal can be treated as the sum of a signal component and a baseline component. Figure 2.8 (a) and (b) show the experimental procedures of the conventional method and the RBC method respectively. For clarity purposes, the total received signal is not shown here. Figure 2.8 (c) and (d) show the final results of these two method, where “corrected baseline”

is the result of the baseline component cancellation for each method. The conventional method collects the whole received signal decay and the baselines afterward separately (Figure 2.8 (a)), then calculates their difference (Figure 2.8 (c)). In contrast, in the RBC method the received signal values at laser "on" and the baseline values at laser "off" states appear alternatively and the difference is immediately measured by the lock-in amplifier for each individual boxcar delay in real-time, as shown in Figure 2.8 (b). By adopting this modulated data acquisition sequence, the RBC method is more capable of suppressing the noise and therefore improves the signal-to-noise ratio. As shown in Figure 2.8 (c) and (d), the conventional method still contains significant oscillation, but the corrected baseline component of the RBC method is much closer to zero. In the conventional method, the measurement of the received signal and the baseline is so far apart (a few seconds), that the baseline has shifted between these two measurements. On the contrary, the RBC method immediately (within a few 10s of μs) takes the baseline values after measuring the received signal values, thus the baseline values can be better conserved before the low frequency baseline fluctuation significantly changes the baseline values.

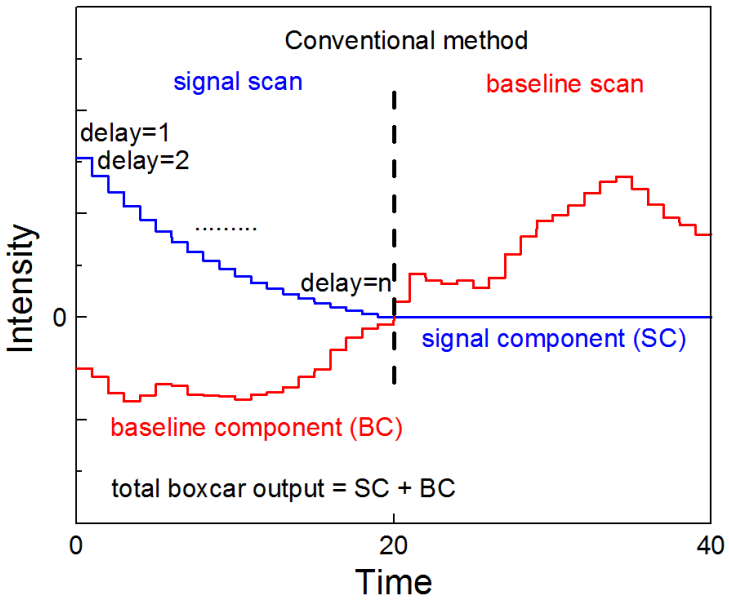
Conventional method
signal scan
baseline scan
delay=1
delay=2
delay=n
signal component (SC)
baseline component (BC)
total boxcar output = SC + BC
Intensity
0
0
20
40
Time

(a)

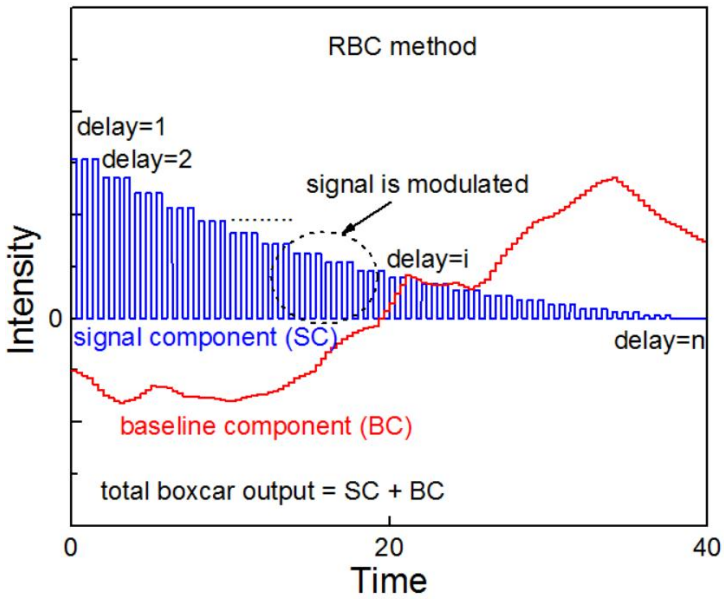
RBC method
delay=1
delay=2
signal is modulated
delay=i
signal component (SC)
delay=n
baseline component (BC)
total boxcar output = SC + BC
Intensity
0
0
20
40
Time

(b)

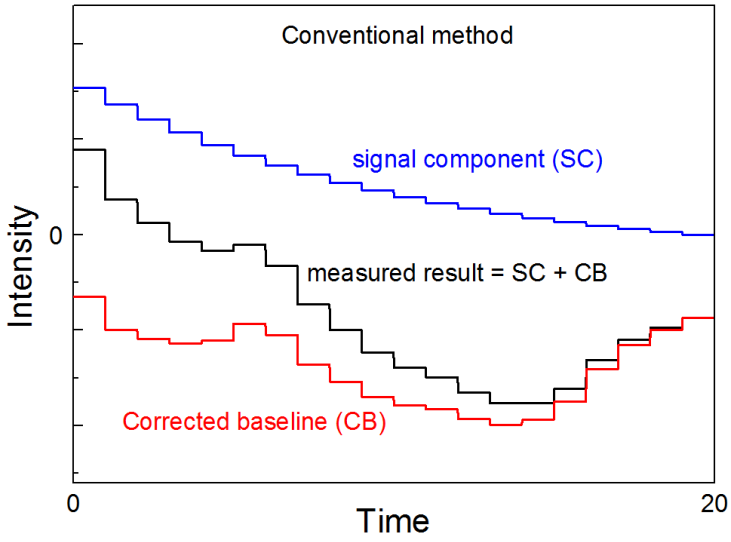

(c)

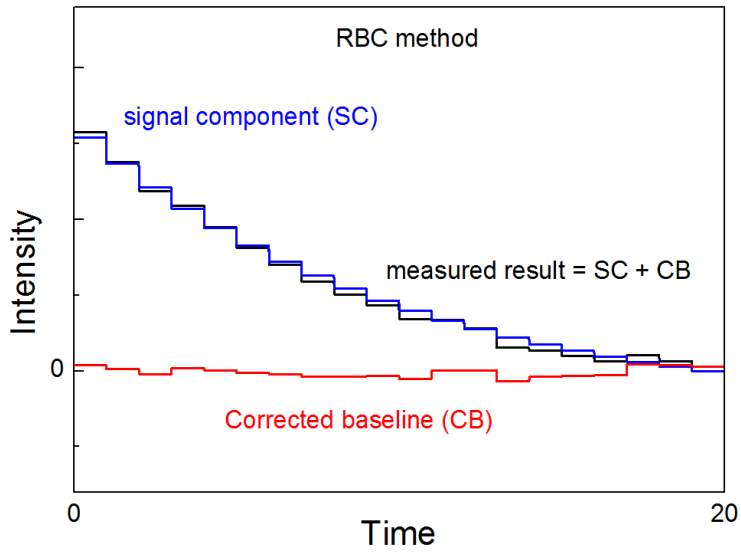

(d)

Figure 2.8. Schematic comparison of the conventional method and the RBC method. (a) The measured result (not shown) by the conventional method is the sum of a signal component and a baseline component. (b) At each boxcar delay, the RBC method modulates the signal and baseline, so that the baseline value is taken immediately after the signal value is measured. (c) The measured result (black curve) of the conventional method deviates from the actual signal component (blue curve). (d) The measured result (black curve) of the RBC method is close to the actual signal component (blue curve).

2.4. Noise Suppression Mechanism

An in depth understanding of the noise suppression mechanism can be achieved by comparing the conventional method with the RBC method in both the time and the frequency domains.

In the conventional method, the single boxcar samplings are averaged over a certain time constant t_0, then the baseline is subtracted from the received signal long after the signal is taken. This is mathematically equivalent to a convolution with a weighting function [32] $f_1(t)$, which consists of a positive pulse and a negative pulse separated by the length of the scan t_s in each period, as shown in the Figure 2.9 (a). In the frequency domain, it is a multiplication with its spectrum $g_1(f)$ as shown in the black curve of Figure 2.9 (b). In order to make it simple and easy to understand, the spectrum can be regarded as oscillations on top of an envelope. The envelope function of $g_1(f)$, which is plotted in Figure 2.9 (b) as the red curve, increases as frequency increases below $1/t_s$, and decreases as $1/f$ at frequencies higher than $1/t_0$, and it is constant between $1/t_s$ and $1/t_0$.

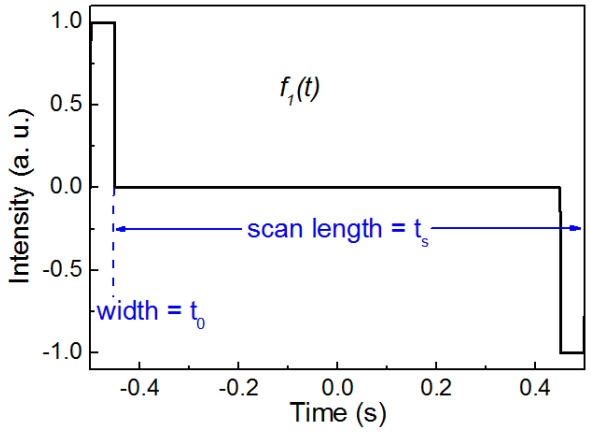

(a)

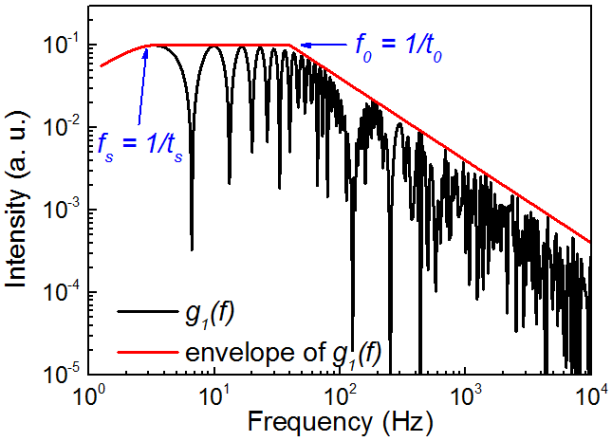

(b)

Figure 2.9. (a) One period of the weighting function in the conventional method and (b) its spectrum. The red curve is an envelope function that guides the eye.

The frequency domain manipulation of the RBC method is understood in two steps. The boxcar sampling outputs immediately enter the lock-in amplifier, which measures the amplitude of the first order harmonic by

$$\text{output} = \frac{1}{T}\int_0^x y(t)\sin(2\pi f_m t)\,dt \tag{2.1}$$

The above expression is equivalent to two mathematical steps. First, it

multiplies the input with a sinusoidal wave, $f_2(t)=sin(2\pi f_m t)$. The frequency is equal to the modulation frequency f_m, which is much higher than $1/t_0$, where t_0 is the average time in the conventional method. The waveform is plotted in Figure 2.10 (a), and the spectrum $g_2(f)$ is a single delta function as shown in Figure 2.10 (b).

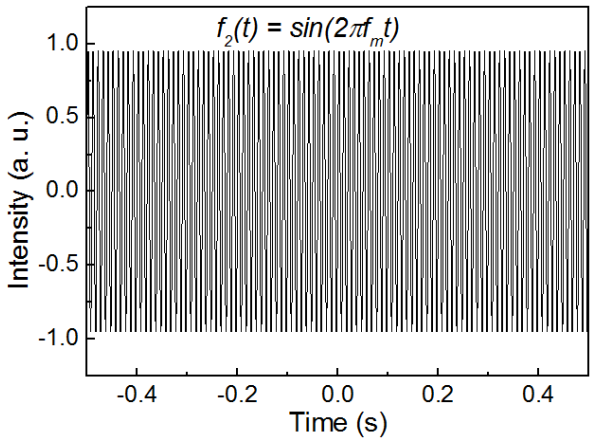

(a)

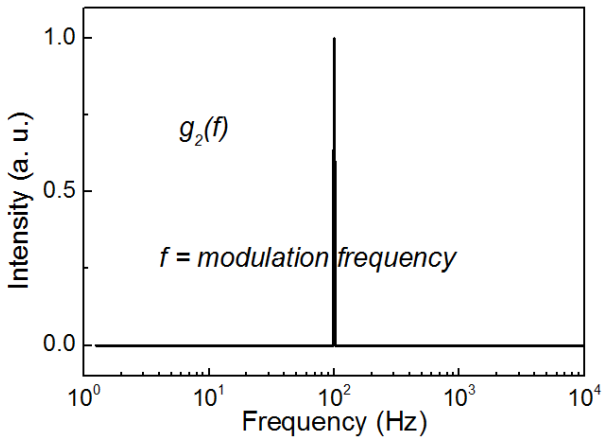

(b)

Figure 2.10. (a) A sinusoidal function with a frequency of f_0 and (b) its spectrum.

The second step is an integration over the time constant T. Mathematically it is

a convolution with a square pulse function $f_3(t)$. The comparison between the RBC method and the conventional method is fair when they have the same measurement time. Since the conventional method measures signal and baseline with a total time of $2t_0$, the integration time (pulse width) here is also $2t_0$. Function $f_3(t)$ is shown in Figure 2.11 (a). In the frequency domain, it processes a multiplication with the spectrum $g_3(f)=2\sin(2\pi t_0 f)/f$, as shown in the black curve of Figure 2.11 (b). An envelope function of $g_3(f)$ is plotted in Figure 2.11 (b) as a red curve. This multiplication performs as a low pass filter which suppresses the high frequency parts.

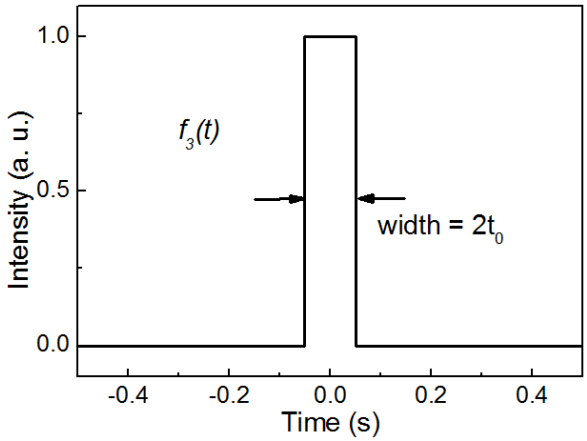

(a)

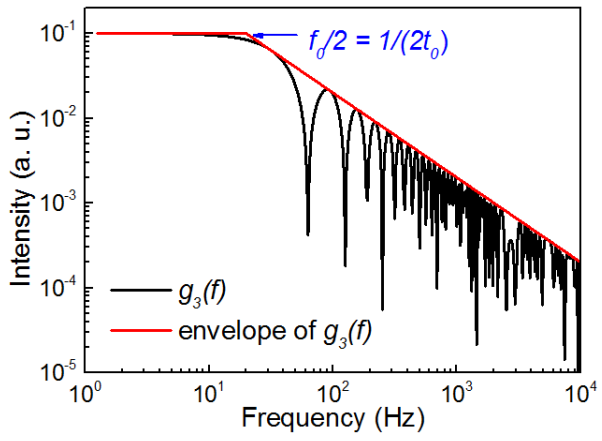

(b)

Figure 2.11. (a) One period of the pulse function with a pulse width of $2t_0$ and (b) its spectrum. The red curve is an envelope function that guides the eye.

The change of the power spectrum of 1/f noise by the core processes of these two methods are compared in Figure 2.12. The black curve is the 1/f noise power spectrum, coming from the boxcar output. The blue curves are the final noise power spectra after going through the previously described processes of Figure 2.10 and 2.11. The red curve is the envelope function of the blue curve for a better visualization. In Figure 2.12 (b), the green curve is the intermediate state when the signal goes through the convolution with the sinusoidal function. The high frequency parts (> 100 Hz) of the final results (blue curves) are similar. On the other hand, in the low frequency parts (< 100 Hz) the noise power of the conventional method Figure 2.12 (a) is higher than that of the RBC method Figure 2.12 (b). This is due to the multiplication with the sinusoidal function in the RBC method "shifts the zero frequency" of the noise to its modulation frequency (green curve in Figure 2.12 (b)), so that the low frequency part can be reduced.

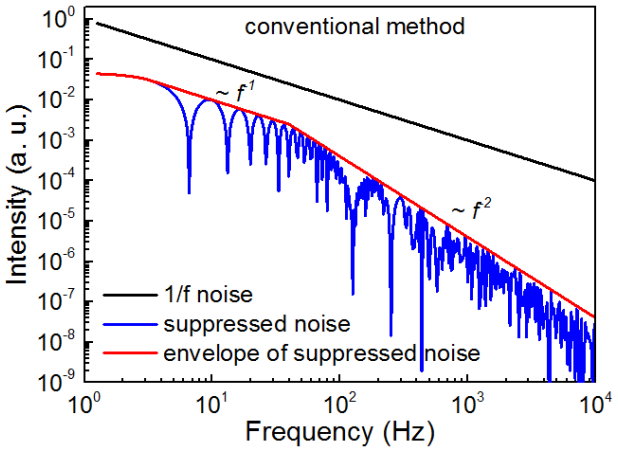

(a)

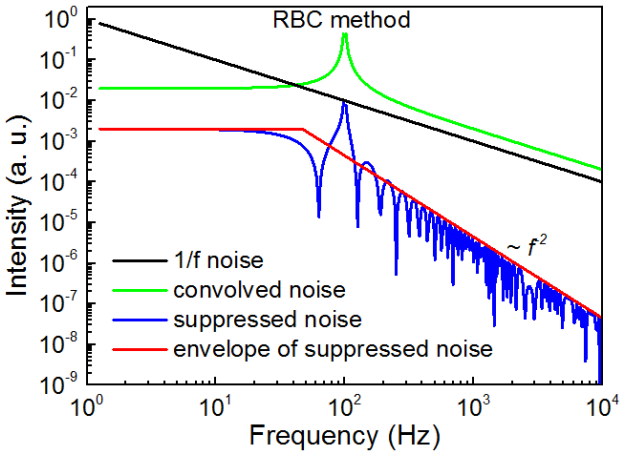

(b)

Figure 2.12. Noise power spectrum of 1/f noise after the measurement of (a) conventional method and (b) RBC method. The black curves are the original 1/f noise power spectrum. In (b) the green curve is the intermediate spectrum after the convolution with the sinusoidal wave in the RBC method. The blue curves are the final noise power spectra. The red curves are envelope functions of the blue curves that guide the eye.

Some discussions of the spectrum analysis results are present in this paragraph. First, the RBC method suppresses both low and high frequency noise due to its

averaging by the lock-in amplifier. Indeed, the lock-in amplifier provides a notch filter in the frequency domain that takes both the signal and noise near the modulation frequency, and reduces the noise at all other frequencies. Second, similar analysis of other types of low frequency noise, including the baseline fluctuation noise in this experiment, also demonstrates that better low frequency noise suppression can be achieved by using the RBC method. The fundamental reason for the better suppression is due to the notch filter in the RBC method removing the low frequency noise. Third, as an additional step, the signal needs to go through a computer sampling process, and it is numerically demonstrated that the final noise power intensity is still proportional to the noise power density at the modulation frequency. When the 1/f noise dominates, the final noise power intensity is proportional to 1/f, so a high modulation frequency allows for better noise suppression. Fourth, the conventional method can be regarded as having a modulation period of the scan length, which is much longer than the modulation period of the RBC method, and therefore is more vulnerable to low frequency noise.

2.5. Simulation of the Noise Suppression

As analyzed previously, the main problem of the conventional TRPL experiment is the low frequency noise, which can be suppressed by the additional modulation introduced by the RBC method. In this section a series of simulations are performed to compare the conventional method with the RBC method, for the purpose

of examining the effectiveness of the RBC method.

An initial simulation compares the output at a fixed boxcar delay, and the details of the simulation are described in this paragraph. The signal intensity is arbitrarily set as 1. The signal and baseline values are sequenced based on the measurement sequence of the conventional method and the RBC method respectively. This sequence is schematically illustrated in Figure 2.13. A 1/f noise is generated and added on top of the signal and baseline. Since 1/f noise is self-correlated, a sequence of noise values covering the scan length is generated, and only the noise during the signal and baseline measurements of the same delay is used for this calculation (see upper part of Figure 2.13). In this simulation the boxcar sampling rate is 10^4 Hz, the modulation frequency is 10^2 Hz, and with a total measurement time of 1 second, including signals and baselines. In this initial calculation, the scan only contains 1 boxcar delay so the scan length is 1 second. For the conventional method, the output is the averaged signal minus the averaged baseline. For the RBC method, the output is the weighted average with the sinusoidal weighting function. To compare different kinds of noise, 1/f, white and blue (power intensity $\sim f$, representing an example of high frequency noise) noises are added to all the data points respectively. For each method, the simulated single measurement is repeated 10^3 times to check the variation that demonstrates the noise in the final measurement.

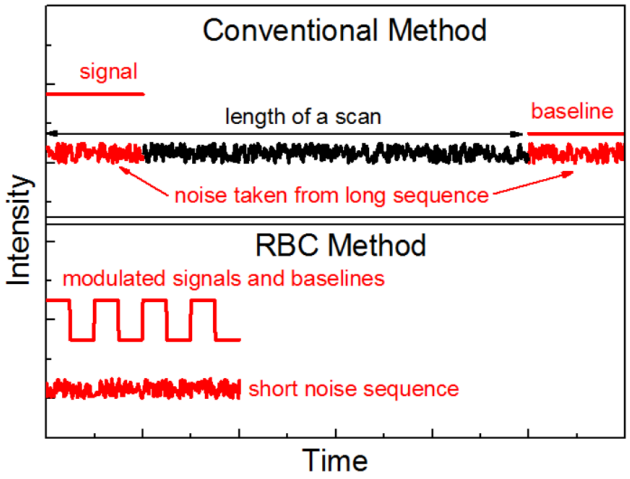

Figure 2.13. Signal, baseline and noise data generation for the simulation of both conventional method and RBC method.

The calculation results are shown in Figure 2.14. For 1/f noise (Figure 2.14 (a)) which is more significant at low frequencies, the RBC method significantly reduces the variation in the measurement compared with the conventional method (Figure 2.14 (b)). For white noise which has an even weight at all frequencies (Figure 2.14 (c)), both methods behave similarly (Figure 2.14 (d)). For blue noise which weighs more at high frequencies (Figure 2.,14 (e)), the RBC method has larger variation than the conventional method (Figure 2.14 (f)). The variances of the output are calculated and shown in Table 2.3. This result shows that the RBC method is more sensitive to high frequency noise than the conventional method. Since the scan length is 1 second, the conventional method has an effective modulation frequency of 1 Hz, so the variance ratios are very close to the ratio of the noise power density of the input noise at the effective modulation frequencies. Therefore, the 1/f noise (low frequency noise) can be

reduced by the RBC method more efficiently than the conventional method.

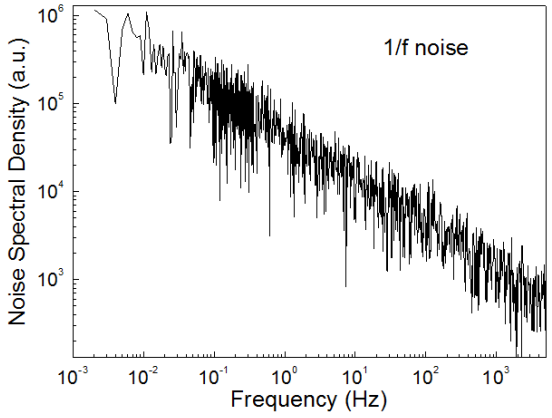

(a)

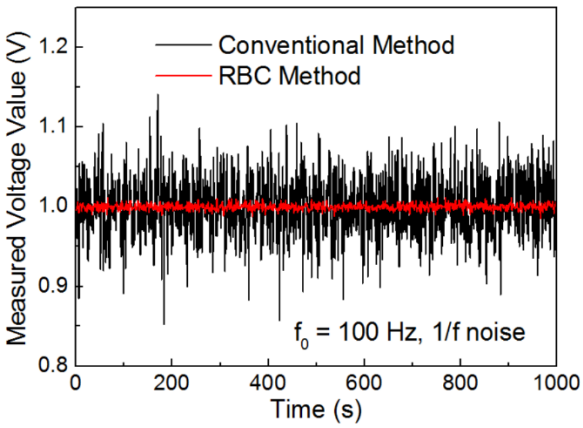

(b)

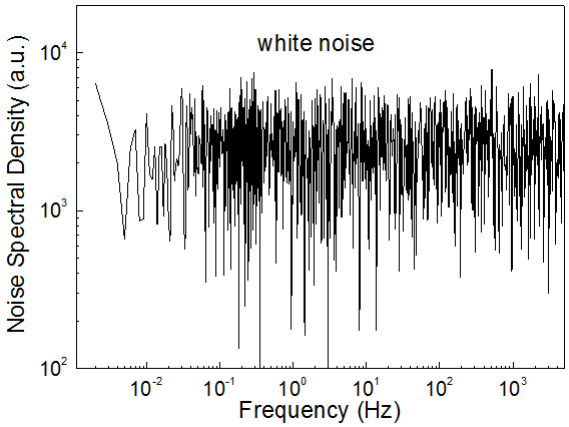

(c)

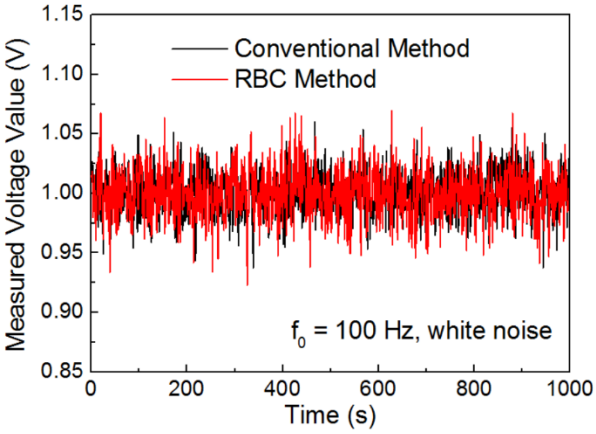

(d)

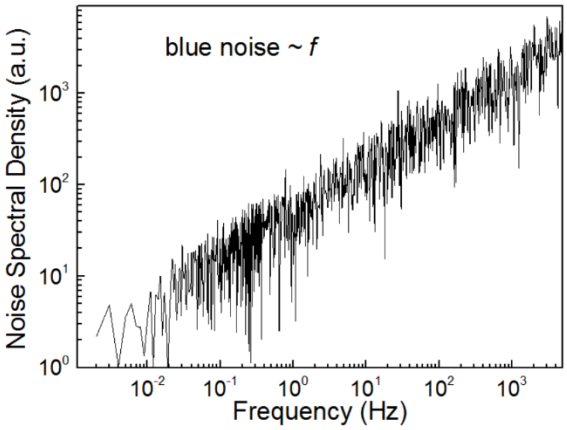

(e)

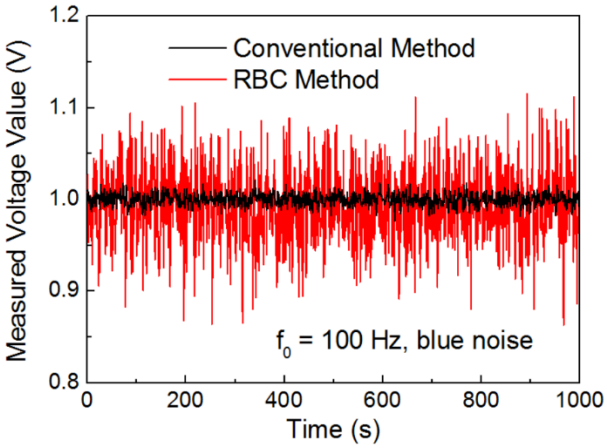

(f)

Figure 2.14. A comparison between the conventional method and RBC method with a modulation frequency of 100 Hz. The results achieved in (b), (d) and (f) use (a) 1/f noise, (c) white noise and (e) blue noise, respectively.

Table 2.3. Comparison between the Variance of the Simulated Results Achieved by the Conventional Method and the RBC Method, with a Modulation Frequency of 100 Hz and Different Types of Noise

Type of noise	1/*f* noise	White noise	Blue noise
Frequency dependence of the noise power density	f^{-1}	f^{0}	f^{1}
$\frac{\sigma^2_{conventional}}{\sigma^2_{RBC}}$	1.03×10^{2}	0.98×10^{0}	1.05×10^{-2}

As a second simulation, the noise at different modulation frequencies in the RBC method are tested with 1/f noise. The results shown in Figure 2.15 demonstrate that at higher frequencies the noise is reduced more efficiently. The variance ratios of the results by these two methods are calculated and shown in Table 2.4. The ratio is proportional to the modulation frequency, confirming the previous conclusion that the noise is proportional to the noise power density of the 1/f noise spectrum at the modulation frequency.

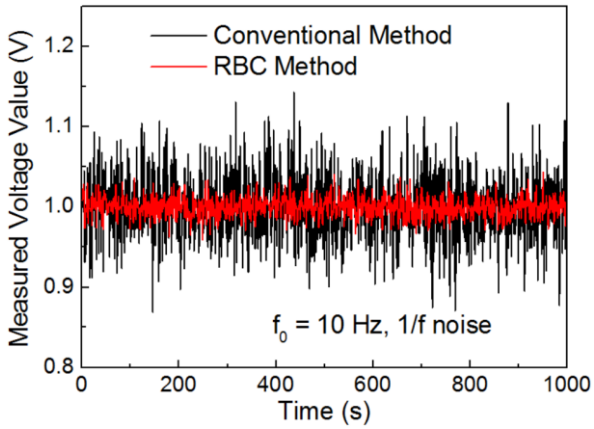

(a)

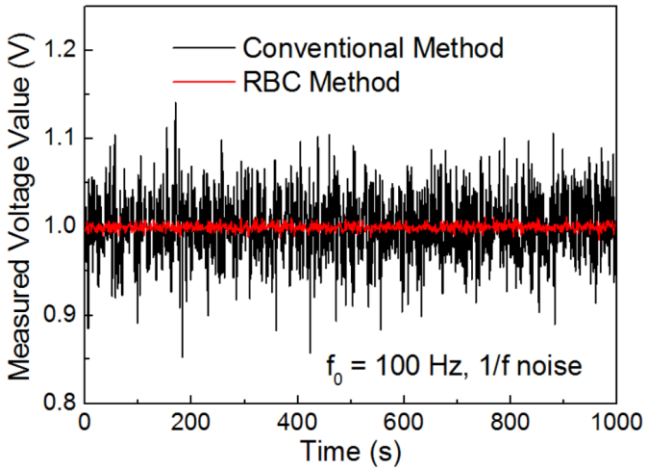

(b)

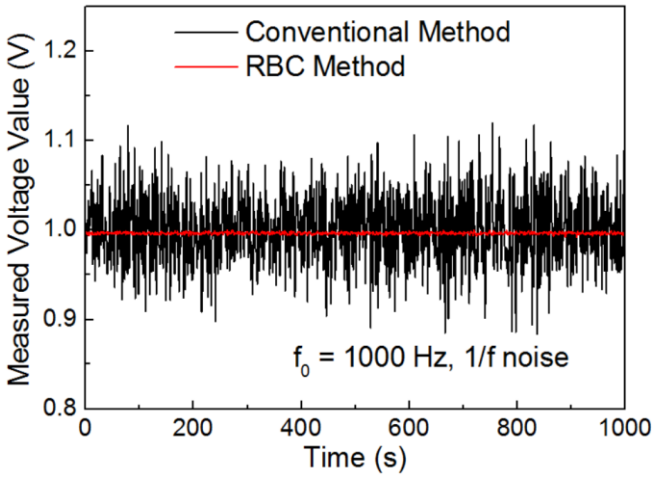

(c)

Figure 2.15. Comparison between RBC method and conventional method, with modulation frequencies of (a) 10 Hz, (b) 100 Hz and (c) 1000 Hz.

Table 2.4. The Variance Ratios in the Simulation Results for the Conventional Method and the RBC Method, with Different Modulation Frequencies under 1/*f* Noise

Modulation frequency (Hz)	10	100	1000
$\frac{\sigma^2_{conventional}}{\sigma^2_{RBC}}$	1.07×10^{1}	1.03×10^{2}	1.02×10^{3}

In the third simulation, a time-dependent signal is introduced to simulate the measurement of an exponentially decaying signal as a function of time. Two types of noise are used separately, representing two dominant noises in this experiment. One noise is 1/f noise, shown in Figure 2.16 (a), the other noise has a power intensity proportional to f^{-6}, as shown in Figure 2.16 (c). The exponent -6 is chosen to be much lower than -1, so that this noise will have a much larger component in the much lower frequency region than the 1/f noise. The behavior may differ from the actual baseline fluctuation noise, but it is useful to demonstrate the situation of very low frequency noise. As shown in Figure 2.16 (b), when 1/f noise dominates, the RBC method gives a clearer exponential decay than the conventional method, while the conventional method gives an exponential decay with significantly larger noise. For the lower frequency noise shown in Figure 2.16 (c), the result in Figure 2.16 (d) shows some slow variation for the conventional method, which makes the decay tail very different from the single exponent. As a comparison, the RBC method gives a much clearer single exponent. Such result suggests that the RBC method is more efficient for different types of low frequency noise than the conventional method.

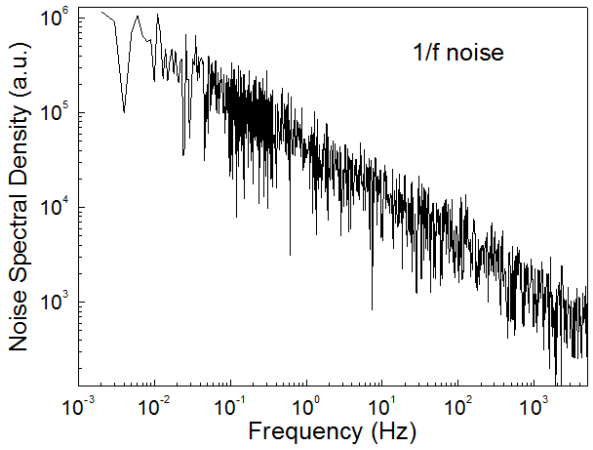
1/f noise
Noise Spectral Density (a.u.)
Frequency (Hz)

(a)

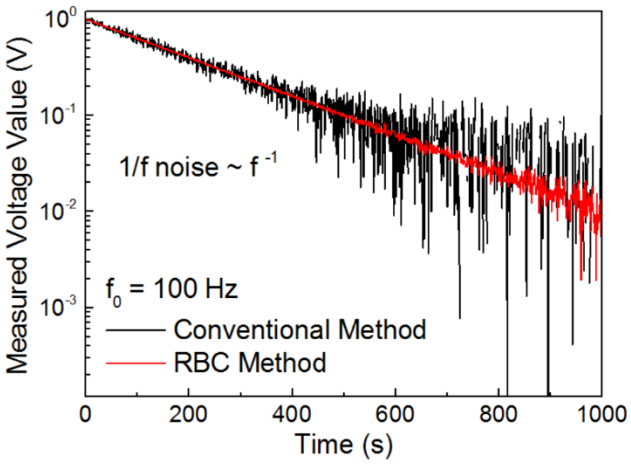
1/f noise ~ f -1
f0 = 100 Hz
Conventional Method
RBC Method
Measured Voltage Value (V)
Time (s)

(b)

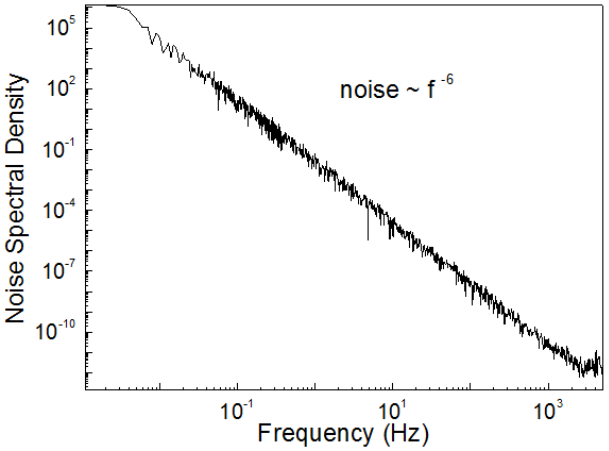
noise ~ f -6
Noise Spectral Density
Frequency (Hz)

(c)

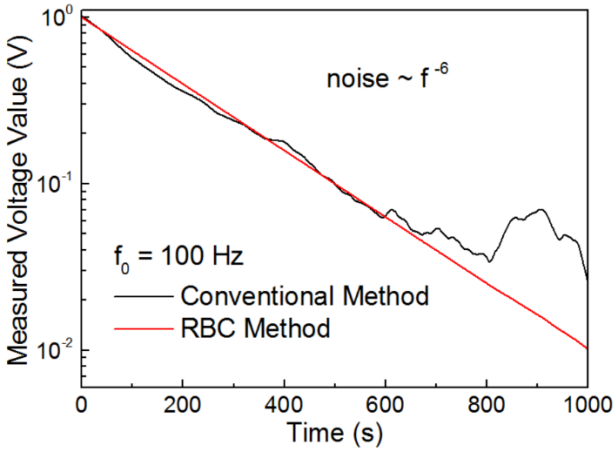

(d)

Figure 2.16. Simulation of a TRPL measurement, assuming the PL signal decays single exponentially, using both the RBC method and the conventional method. With a 1/f noise shown in (a), the results are shown in (b). With a noise $\sim f^{-6}$ shown in (c), the results are shown in (d).

To summarize this section, the simulation results suggest that the RBC method is sensitive to the noise at modulation frequency, and can suppress noise of other frequencies. As a result, low frequency noise can be suppressed more efficiently by the RBC method since it has a larger effective modulation frequency than the conventional method.

2.6. Performance

The superior performance of the RBC method is confirmed by experimental results. The desired TRPL signals obtained using the conventional and the RBC methods are shown in Figure 2.17 on the same sample with identical conditions. The

results obtained using the RBC method with two different modulation frequencies are also compared. As in Figure 2.17, using the conventional method (black dots), the TRPL signal possesses multiple oscillations over the timescale of 0.5 μs to 1.5 μs, caused by the low frequency baseline fluctuation induced by the laser pulse. On the other hand, using the RBC method (red and blue dots) these oscillations are completely removed. The RBC method with a modulation frequency of 100 Hz suppresses the standard deviation of the dominant noise by 60 % after 6 μs, as compared to the conventional method. With a modulation frequency of 800 Hz, the RBC method further suppresses this noise by 70 %. The TRPL signal from 1.5 μs to 4.5 μs, which was buried in the noise using the conventional method, is now resolved clearly by using the RBC method. This improved experimental method resolves the weak TRPL signal buried in the noise in short time, making it more practical for the TRPL measurements of infrared materials.

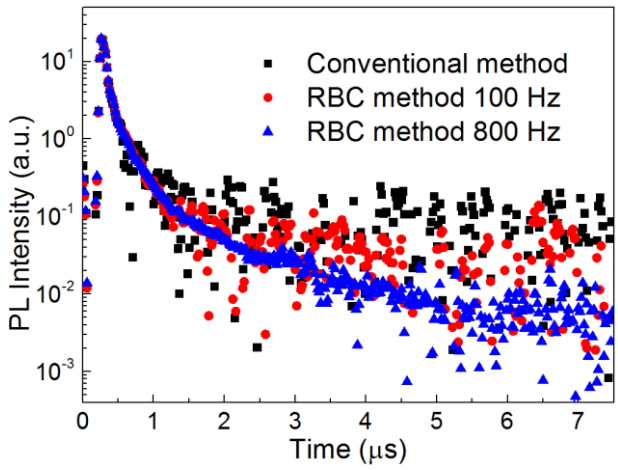

Figure 2.17. Comparison between the TRPL signals measured by the conventional

method and the RBC method with modulation frequencies of 100 Hz and 800 Hz. These signals are collected on the same sample with identical conditions. The RBC method not only removes the baseline fluctuations between 0.5 μs and 1.5 μs, but also suppresses the noise at decay times greater than 6 μs. Using the 800 Hz modulation frequency, the noise is further suppressed compared with 100 Hz.

2.7. Discussions

It is desirable to use the RBC method with a high modulation frequency, but the modulation frequency must satisfy certain conditions. First, the modulation frequency f_0 cannot be higher than the boxcar sampling frequency. The boxcar sampling period has to be long enough to cover the complete PL decay after each excitation, so that the lifetime of interest can be accurately resolved, therefore the upper limit of the modulation frequency is related to the lifetime of interest. For example, in this TRPL experiment, the longest lifetime of interest is on the order of 10 μs, and a boxcar delay scanning range of at least 100 μs has to be chosen, thus a modulation frequency of at most the reciprocal of 100 μs (10 kHz) can be used. Second, as a practical issue, depending on the position of the chopper blade and the phase of the laser pulse, the number of pulses in each chopping period can vary by 1 from period to period. This issue can be resolved by setting the ratio between the pulse frequency over the modulation frequency to an accurate integer N by using an extra circuit for synchronization. As an alternative practical solution for this issue, the modulation frequency can be set much lower than the pulse frequency, and this issue can be

alleviated as the small difference between the number of pulses in each period leads to negligible measurement error.

A more efficient approach with the highest possible modulation frequency in the RBC method can be achievable with better synchronization devices. In our demonstration of the RBC method, since the chopper cannot be synchronized with the pulse laser (10 kHz), the modulation frequency has to be set much lower than the frequency of the pulse laser. However, some non-mechanical choppers such as acousto-optical modulators or electro-optical modulators can be modulated at much higher frequency. It is possible to use those choppers to bring the modulation frequency up to the laser pulsing frequency and further reduce the noise.

The RBC method is not only useful for the TRPL experiment, but also can be applied to any boxcar-based time-resolved experiments that suffers from low frequency noise and have baselines repeating at the frequency of the external excitation such as laser pulse in this case.

2.8. Summary

The noise issues in a TRPL system using a conventional method is analyzed, revealing that the total noise is dominated by low frequency noises, including 1/f noise and baseline fluctuation noise. The RBC method is proposed to suppress the signal-to-noise ratio. The RBC method is realized by modifying the conventional TRPL system with a chopper and a lock-in amplifier. The noise suppression is supported by both the

analysis in the frequency domain and the computer simulation. The improved signal-to-noise ratio of the RBC method is confirmed by experimental results. After this improvement, the signal-to-noise ratio of the TRPL measurement is significantly enhanced by 2 orders of magnitude and the signal decay with lower PL intensity, which can provide critical information but was previously buried in the noise of the conventional method, can be resolved using the new method more efficiently. This RBC method is used for TRPL measurements to determine the minority carrier lifetimes in Chapters 3 and 4.

3. CARRIER LOCALIZATION IN INAS/INASSB TYPE-II SUPERLATTICES

One significant advantage of InAs/InAsSb type-II superlattices (T2SLs) over InAs/InGaSb T2SLs is the low Shockley-Read Hall (SRH) recombination rate, which leads to a long minority carrier lifetime [20]. Optical approaches, such as TRPL [20], time-resolved differential transmission [21] and optical modulation response [27], have been used to measure minority carrier lifetimes in InAs/InAsSb T2SLs. The lifetimes have been reported to be as long as 412 ns in the long-wavelength infrared (LWIR) regime [20][33], 9 μs [21], 10 μs [22] and 12.8μs [23] in the mid-wavelength infrared (MWIR) regime at 77 K under low excitation conditions. These reported lifetime values are much longer than the ~ 30 μs [17][18][19] measured in InAs/InGaSb T2SLs, which is a result of the low SRH recombination rate [20]. Long minority carrier lifetime is therefore regarded as an indicator of good device performance in InAs/InAsSb T2SL photodetectors, because a low SRH recombination rate leads to a high photo-generated carrier extraction efficiency and a low dark current [34]. However, it is reported that the radiative recombination dominant minority carrier lifetime in a MWIR InAs/InAsSb T2SL is only 2.8 μs at 77 K, with a carrier concentration of 1.5×10^{15} cm^{-3} [35]. Since the radiative recombination is intrinsic, this suggests that the long minority carrier lifetime may not be purely due to the reduced SRH recombination rate, and there are other factors that influence the minority carrier lifetime. Since the minority carrier lifetime is a key parameter for optimizing the InAs/InAsSb T2SL photodetector, its

origin needs to be carefully investigated.

This chapter demonstrates that the long minority carrier lifetime in MWIR InAs/InAsSb T2SLs are influenced by strong carrier localization at low temperatures. Carrier lifetimes measured using optical approaches can be greatly enhanced by carrier localization [36] which has been widely observed in semiconductor materials [36][37][38][39][40]. When carrier localization is strong, spatially indirect SRH recombination dominates the non-radiative recombination in optical measurements [40], but generation-recombination (GR) dark current usually follows the trend $J_{GR} \sim (\tau_{GR})^{-1}$, where τ_{GR} is the spatially direct SRH generation lifetime in the depletion region. Under the influence of carrier localization, the GR dark current is underestimated if calculated using the optically measured carrier lifetime. Moreover, in the case of strong carrier localization, carrier transport is inhibited [39] and the photo-generated carrier extraction efficiency could potentially be diminished. It is therefore important to identify whether carrier localization exists, so as to properly design and evaluate the InAs/InAsSb T2SL photodetectors using the optically measured carrier lifetimes.

3.1. Carrier Localization

Carrier localization is a common phenomenon in semiconductors, originating from the disorder in solids. The properties of an ideally ordered system is relatively easy to solve since the quantum objects have Bloch-type wave functions which are periodical throughout the whole space. However, in reality materials always contain

disorders such as impurities, vacancies, dislocations and other defects. These disorders have a significant impact on some of the material properties. Since the 1970s, thanks to bigger and faster computers, numerous theoretical methods have been used to study the electronic properties of disordered solids. At the same time, emerging experiments are employed to verify or falsify these theories.

One important and extensively studied field of carrier localization is the influence of disorder on the transport properties in condensed matter systems [41]. The one-particle wave functions in the disordered system decays exponentially in space when the level of disorder is sufficiently strong. If the particles are in states with exponentially decaying wave functions in space, they are restricted to a finite region and cannot contribute to the transport without the interaction with other particles such as phonons. These states are called localized states. On the other hand, if the disorder is weak, or the eigen-energy of the state is high, the wave functions are more likely to extend throughout the whole space, with fluctuating intensities and phase near the disorder, and these states are known as extended states. Only the particles in the extended states can transport spatially. If the Fermi edge is below the mobility edge, as shown in Figure 3.1, close to the localized states, the transport will be limited. Even if the Fermi edge is near the extended states, i.e. in the metallic regime, the disorder serves as a scattering center, leading to an increasing resistance. For these reasons, there could be significant influence from disorder and localized states on the semiconductor device

operation.

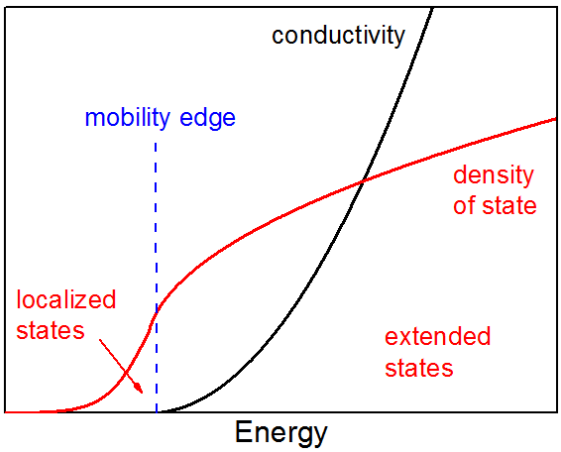

Figure 3.1. Scheme of mobility edge and localized states, originally from reference [41].

When the Fermi level is below the mobility edge, the bottleneck to carrier transport is the thermal activation from the localized states into the extended states, so the mobility is inversely related to the temperature. When temperature is near 0 K, the hopping process becomes the dominant transport process [41], which can be described by the "Mott's $T^{-1/4}$ law" [42][43]. In Mott's theory, the hopping process is assisted by phonons, and the hopping probability is exponentially related to the percolation parameter, which are determined by the wave function overlap between two localized states, and the energy difference between these two states [44].

Recently, the carrier localization has also been studied using pure optical approaches. Carrier transport properties of an intentionally disordered GaAs/AlGaAs superlattice are studied by observing the PL of the bottom layer. After comparing the superlattices with different degrees of disorder, it is concluded that the transport is

inhibited in the disordered superlattices [39]. A significant characteristics of carrier localization in a disordered semiconductor is the “S-shaped” PL peak energy as a function of temperature, shown in Figure 3.2 (a). In a disordered system, the localized state energy distributes randomly. As shown in Figure 3.2 (b), when temperature is near 0 K (blue), most carriers cannot be thermally excited outside the localization centers with randomly distributed energies. As temperature increases (green) the carriers in the shallow localization centers can be thermally excited, and fall into deep localization centers. Since most carriers are in the localization centers at these temperatures, the PL is mainly due to the transition between these localization centers, and the PL peak shows a red shift. As temperature increases more (red), the carriers in the deep localization centers are also thermally excited into the extended states, and therefore, the PL peak energy shows a blue shift. As temperature further increases, the band gap shrinkage leads to a PL peak red shift again. Such S-shaped PL peak energy is observed in many material systems, including GaInNAs quantum wells [40][45], InGaN/GaN quantum wells [36], AlGaN quantum wells [46], GaInP [37][47][48], GaAs/AlGaAs system [49][50], AlAs/AlGaAs superlattices [51], InAlAs [52], AlInAs [38]. The S-shape is related to [37][38][50] and well-explained [40][45] by carrier localization. The disordered material is compared with ordered material, and this confirms that the S-shape is unique to the disordered systems [50][51]. Photoreflectance [37][47], PL excitation [38] or optical absorption [50] experiments are also performed to measure

the band gap energy, confirming that the PL peak shift is not due to the band gap shrinkage. This S-shaped relation between the PL peak energy and temperature is regarded as an indicator of carrier localization.

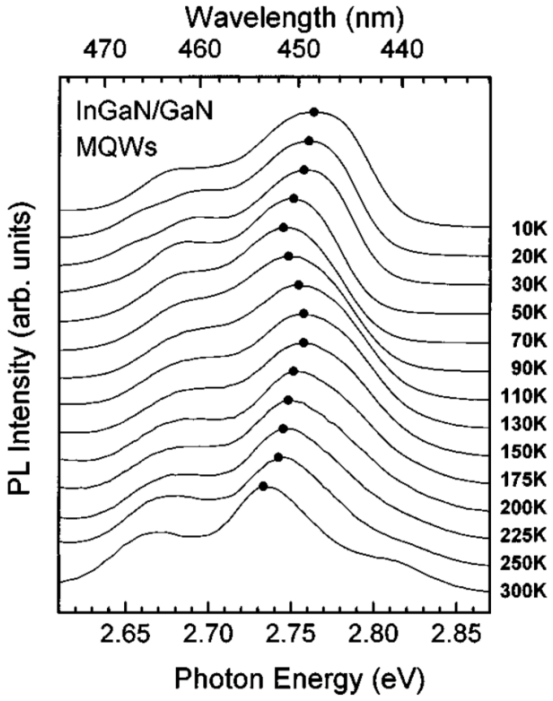

(a)

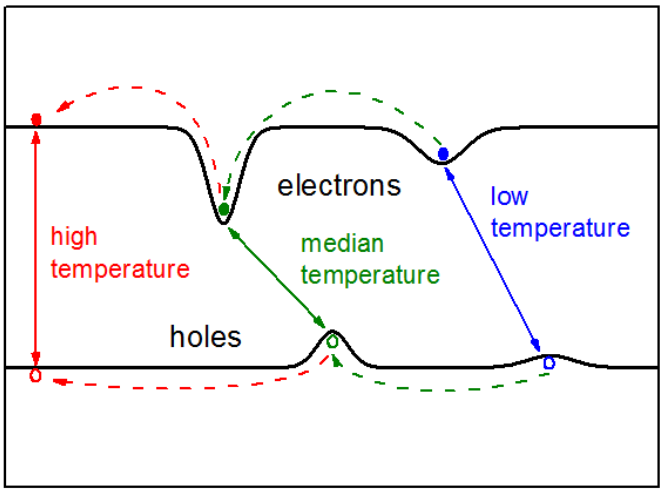

(b)

Figure 3.2. (a) An example of the inverted S-shape PL peak energy as a function of

temperature from reference [36], and (b) its origin. At low temperatures the localized states do not exchange carriers. As temperature increases, the carriers in the shallow localized states are thermally excited, and eventually captured by deep localized states. As temperature further increases, the carriers are thermally excited into the extended states, and the PL peak energy follows the band gap shrinkage.

The PL line width also has an anomalous behavior associated with the PL peak energy shift, as the PL peak blue shifts, the line width decreases, as the PL peak red shifts, the line width increases [36][52]. This behavior is mainly due to the broadening of the high energy side of the PL spectra, related with carrier localization. As shown in Figure 3.3 (a), at low temperatures most of the carriers are distributed in the localized states. The exchange of carriers between the localized states is difficult, resulting in different Fermi levels at different localization centers. The trapped excess carriers follow the statistical distribution of the localization energy instead of a global Fermi distribution, which broadens the PL spectra. As shown in Figure 3.3 (b), at high temperatures when carrier localization does not occur, many carriers occupy the extended states, and the high energy side of the PL spectrum is dominated by the Fermi-distribution of carriers, leading to a steep slope and narrow line width. In the temperature range where the carriers are thermally excited out of the shallow localized states into the deep localized energy states, it also leads to a broadening of the PL peak because of the more populated deep localized energy states.

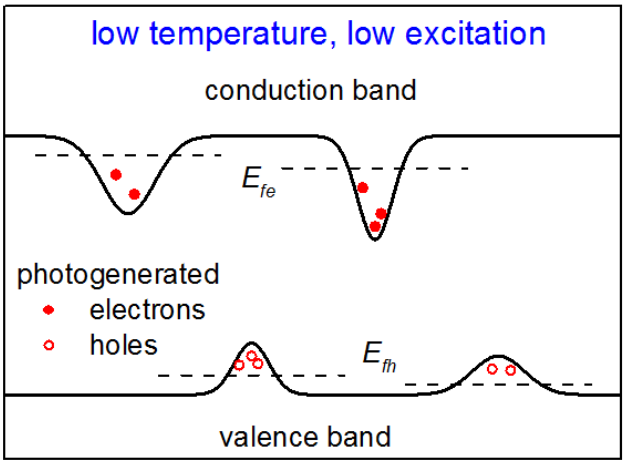

(a)

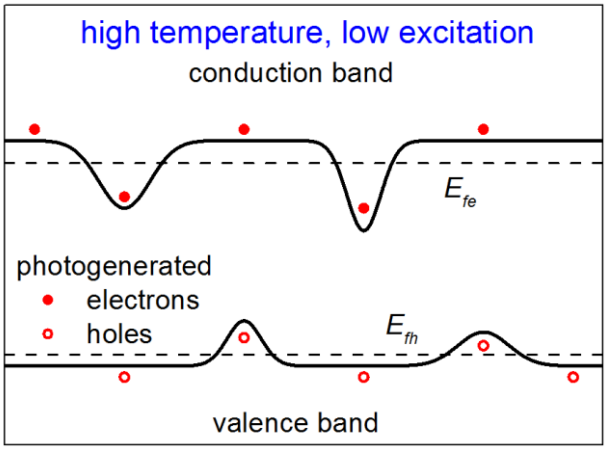

(b)

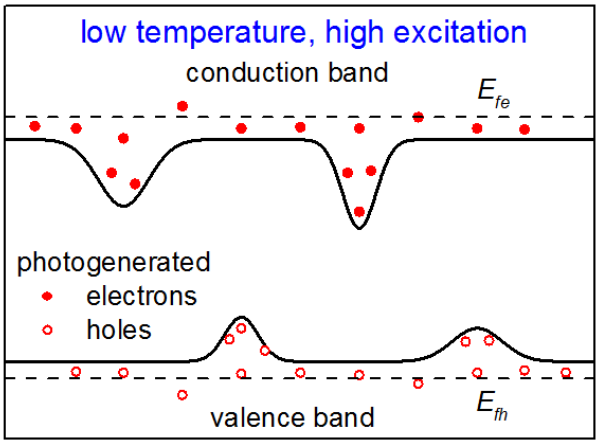

(c)

Figure 3.3. Excess carrier distribution in the disordered semiconductor. (a) At low temperatures, different localization centers do not exchange carriers, therefore the

Fermi levels in different localization centers are different and the carriers do not obey a global Fermi distribution. (b) When temperature is high, the carriers in the localization centers have enough thermal energy to overcome the barrier and occupy the extended states. (c) If excess carrier concentration is high, all the localized states are occupied and the excess carriers begin to fill the extended states, in the cases (b) and (c) the high energy carriers follow a global Fermi distribution.

Even though carrier localization occurs at low excitation densities, the shape of the PL spectra changes with high excitation densities. As excitation density increases, shown in Figure 3.3 (c), the localized states become filled and some extended states are occupied. In this case a global Fermi-distribution can be achieved, and the high energy side of the PL spectrum has the shape of a Fermi-distribution.

When carrier localization occurs, the minority carrier lifetimes are long, but as temperature increases, the long lifetime decreases very sharply [36]. At low temperatures, the dominant transition occurs between those localized states that capture most of the excess carriers. The schematic wave functions of the extended states and the localized states are shown in Figure 3.4. The wave function overlap between these localized states is small, leading to a small transition probability and long carrier lifetime. As temperature increases, more carriers are populated into the extended states with larger wave function overlap, leading to the rapid decrease of carrier lifetime.

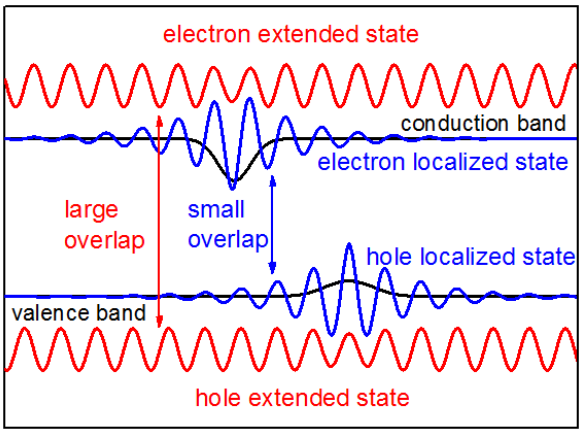

Figure 3.4. The wave functions of the electron and hole for both extended and localized states. The large wave function overlap between the extended states leads to a high transition probability. The small wave function overlap between the localized states leads to a low transition probability and thus, a long minority carrier lifetime.

In the following sections, experimental evidence demonstrates the existence of carrier localization in InAs/InAsSb T2SLs. As illustrated in Section 3.3, the most probable origin of carrier localization is the interface atomic layer fluctuation in the superlattice, confirmed by calculations. This observation is similar to that previously observed in GaAs/AlGaAs quantum wells, where interface roughness leads to carrier localization [49]0.

3.2. Experimental Evidence of Carrier Localization in MWIR InAs/InAsSb T2SLs

Three groups of samples are grown by solid source molecular beam epitaxy on (100)-oriented GaSb substrates, and are outlined in Table 3.1. Group A contains bulk InAsSb lattice-matched to GaSb, group B contains InAs/InAsSb T2SLs with periods

shorter than 12 nm, and group C contains InAs/InAsSb T2SLs with periods longer than 18 nm. These superlattices are designed to be strain-balanced to the GaSb substrate as described in [53]. Detailed growth conditions were previously reported [20][54][55]. Group A has an Sb mole fraction of 0.09, and is lattice-matched to the GaSb substrate. All samples have 500-nm-thick GaSb buffer layers to smooth the substrate surface. The absorber layers are sandwiched between 10-nm-thick AlSb barrier layers which provide confinement for the photogenerated carriers in the PL experiments. The entire structure is capped with 10 nm of GaSb (group A and non-IQE samples in group B) or 10 nm of InAs (IQE samples) to prevent oxidation of the upper AlSb layer. An example of high-resolution x-ray diffraction (XRD) in the (004) direction is shown in Figure 3.5, confirming that the superlattices are closely strain-balanced to the GaSb substrate. The total thickness of the superlattice varies from 500 nm to 1000 nm. These T2SLs are unintentionally n-type doped and chapter 4 demonstrates that the minority carrier (hole) diffusion lengths are longer than 2400 nm below 77 K, much longer than the thickness of the T2SLs, ensuring a uniform carrier distribution for steady state experiments. The PL spectra are therefore not influenced by the layer thickness after calibrating the excess carrier concentration. The minority carrier lifetime is not influenced by the layer thickness as it is determined at the tail of the TRPL curve (excited by a pulse laser) at low excitation densities, where the carriers already reach a quasi-uniform distribution.

Table 3.1. Summary of the Sample Structures

Group	Sample	Wave band	No. of Periods	d_{InAs} (nm)	d_{InAsSb} (nm)	x_{Sb}
A	B1784	-	1	0	1000	0.09
B	B1856	MWIR	90	9.0	2.6	0.30
	B1875	MWIR	100	5.2	4.7	0.19
	IQE29	LWIR	59	6.8	1.8	0.40
	IQE43	LWIR	71	5.7	1.5	0.40
C	IQE33	LWIR	29	17.0	7.2	0.27
	IQE44	LWIR	21	12.5	4.9	0.29

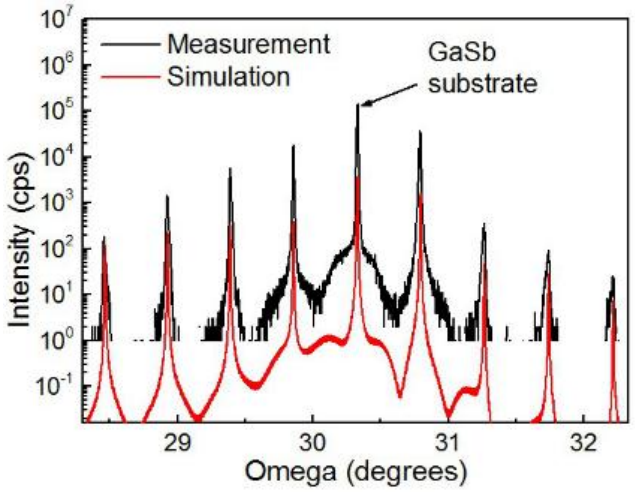

Figure 3.5. (004) X-ray diffraction of sample B1875, the zeroth peak of superlattice overlaps with GaSb substrate peak, indicating the superlattice is strain-balanced to the substrate.

Samples from the same group behave similarly in terms of the PL spectra and minority carrier lifetimes. In the following discussions, only the experimental results of

B1784, B1875 and IQE33 are discussed, representing group A, group B, and group C, respectively, and they will be referred to as sample A (B1784), sample B (B1875) and sample C (IQE33).

Strong evidence of carrier localization is revealed by steady-state PL measurements carried out using a Fourier transform infrared spectroscopy (FTIR). The samples are excited using an 808 nm laser with an excitation density of 0.05 W/cm^2. Using such a relatively low optical excitation density ensures that the excess carrier densities in all the samples are much less than the unintentional background n-type doping of ~2×10^{16} cm^{-3} [20], close to the detector working conditions. The PL peak energies and full-width at half maximums (FWHM) of samples A, B and C are plotted as a function of temperature in Figure 3.6. The Varshni empirical expression can be used to fit the temperature dependence of the PL peak energy for samples A and C, as shown by the solid lines in Figure 3.6. For sample B, however, the Varshni expression only fits the data in the temperature range above 50 K. As temperature increases from 15 K to 50 K, the PL peak energy shows a significant blue shift of 3 meV, much larger than the error bar limited by the FTIR system resolution of 0.25 meV. The FWHMs in the PL spectra of sample A and sample C increase monotonically as temperature increases, but the FWHM of sample B shows the opposite trend below 40 K. As described in Section 3.1, this behavior is a strong indication of carrier localization. At low temperatures and low optical excitation densities, the photo-generated electrons

and holes are bound at these spatially separated localization centers, and the optical transition occurs between electron and hole localized states with corresponding lower transition energies and probabilities. As temperature increases, carriers are thermally excited into the extended states, and the PL peak shifts to higher energies. As the temperature increases further, the carriers predominately populate the extended states, and the PL peak energy shifts to lower energies as the bandgaps of the superlattice constituents become smaller.

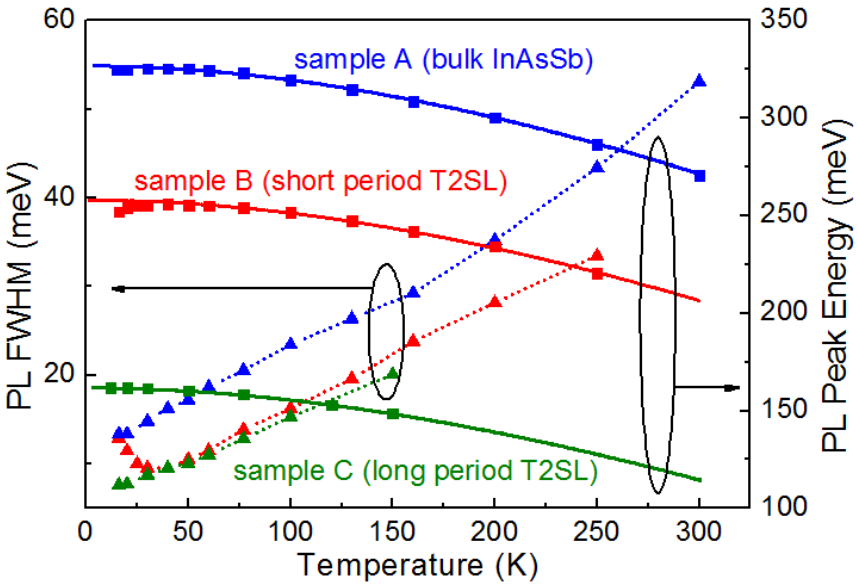

Figure 3.6. PL peak energy and FWHM of samples A (bulk InAsSb), B (short period InAs/InAsSb T2SL) and C (long period InAs/InAsSb T2SL) as a function of temperature. As temperature increases from 15 K to 50 K, the peak energy of sample B increases by 3 meV and the FWHM decreases by 3 meV, indicating carrier localization. The solid lines show the Varshni fit of the PL peak energy as a function of temperature.

At low temperatures, the PL linewidth broadens with decreasing temperature when the carriers are localized. This phenomenon is due to the broadening of the high energy side of the spectra. Excitation dependent PL experiments shed more light on this. The PL spectra are plot on the logarithmic scale in Figure 3.7 (a) and (b). As shown in Figure 3.7 (a), at 15 K, for sample B, when the excitation density is high, the high energy side of the PL spectra follows the Fermi distribution with a slope of ~ e/kT. However, when excitation density decreases, the slope on the high energy side gradually decreases, deviating from the Fermi tail. As a comparison, sample C does not exhibit any carrier localization at 15 K, and in Figure 3.7 (b), as excitation density gets lower, the high energy side of its PL spectra always follow Fermi distribution. These slopes are calculated and shown in Figure 3.7 (c). These phenomena in sample B endorse the existence of carrier localization.

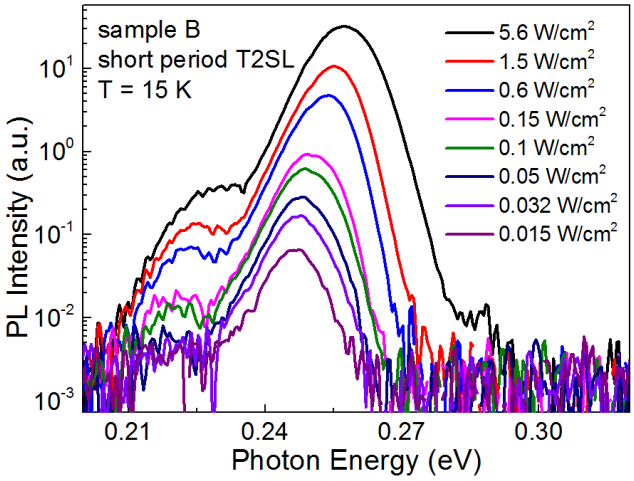

(a)

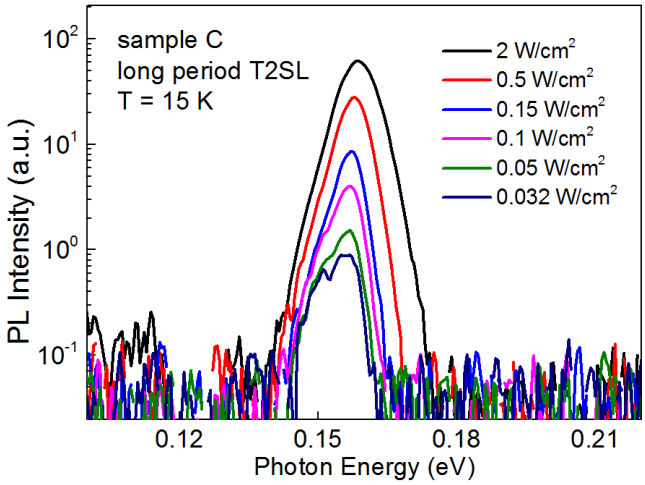

(b)

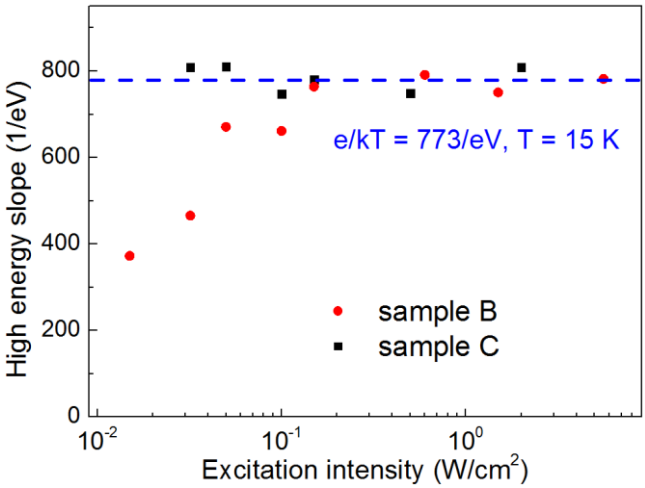

(c)

Figure 3.7. Excitation power dependent PL spectra of (a) sample B and (b) sample C on the logarithmic scale. The slopes of the high energy sides on these spectra are shown in (c).

The minority carrier lifetimes of samples A (bulk InAsSb alloy) and B (short period InAs/InAsSb T2SL) are measured using TRPL at 15 K. The samples are excited using a Nd:YAG pulsed laser with a wavelength of 1064 nm. The luminescence is collected using a liquid nitrogen cooled HgCdTe detector with a time resolution of 20

ns. The transient integrated PL decay signal is measured and processed using the RBC method described in Chapter 2. The measured PL decays shown in Figure 3.8 become single exponential after 1.5 μs and 8 μs, following the laser excitation pulse for samples A and B, respectively. The lifetimes extracted from the single exponential decays are 1.24 μs for sample A, and 12.8 μs for sample B. The TRPL measurement of sample C is reported elsewhere 0[33], showing a minority carrier lifetime of 280 ns at 11 K. Even though a very long minority carrier lifetime of 12.8 μs is discovered in sample B at 15 K, as discussed in Section 3.1, if carrier localization occurs, the photo-generated electrons and holes recombine through spatially separated localized states. The small wave function overlap between these low-energy states, which leads to a low optical transition probability at low temperatures, thus may lead to a minority carrier lifetime of 12.8 μs 0, much longer than that of samples A and C.

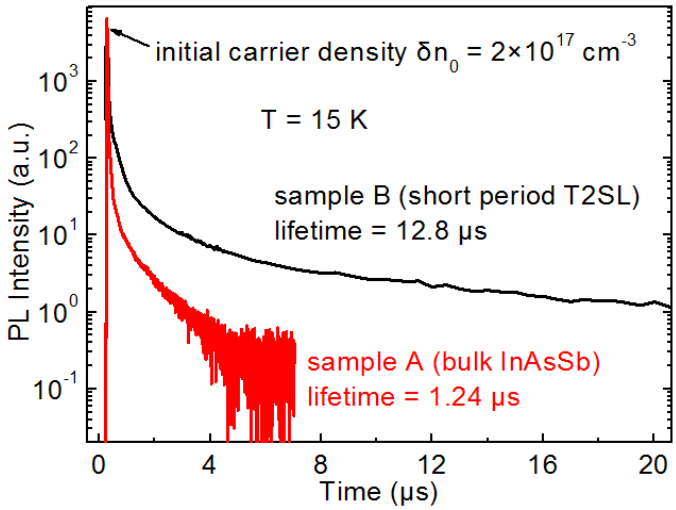

Figure 3.8. TRPL decays of the bulk InAsSb alloy (sample A) and the short period InAs/InAsSb type-II superlattice (sample B) at 15 K. The minority carrier lifetimes are

determined to be 1.24 μs and 12.8 μs respectively.

The temperature dependence of the minority carrier lifetime is measured. If carrier localization occurs, as temperature increases, more carriers are populated into the extended states, with larger wave function overlap, leading to the rapid decrease of carrier lifetime. This temperature dependence is experimentally observed as shown in Figure 3.9. In Figure 3.9 (a), under the influence of carrier localization, the long minority carrier lifetime of sample B at 15 K decreases rapidly as temperature increases. The minority carrier lifetime decreases by an order of magnitude as the temperature increases from 15 K to 77 K. As a comparison, in Figure 3.9 (b), the carrier lifetime of sample C decreases as the temperature reduces below 77 K by the increasing radiative recombination rate.

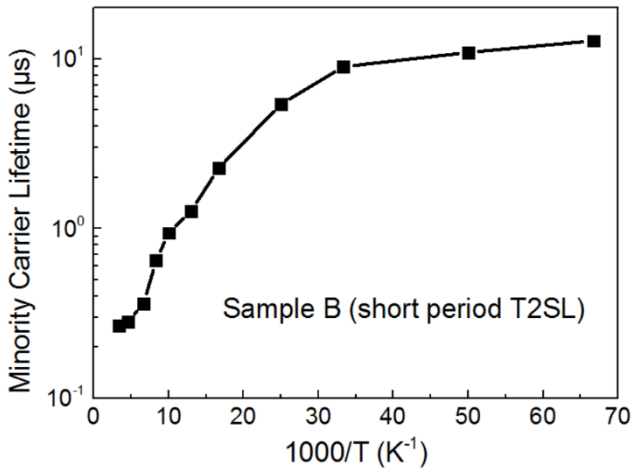

(a)

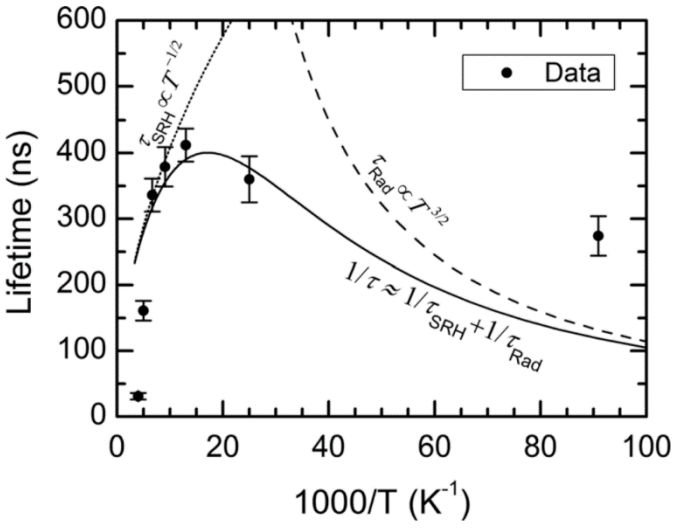

(b)

Figure 3.9. Minority carrier lifetimes as a function of temperature in (a) sample B and (b) sample C. Figure (b) is from [20].

The long minority carrier lifetime at 15 K and its temperature dependence of sample B differs from sample C, consistent with the descriptions of carrier localization in Section 3.1, endorsing the existence of carrier localization at 15 K in group B samples. Along with the strong indications of carrier localization revealed by PL measurements, it is concluded that strong carrier localization occurs in sample B below 50 K.

3.3. Origin of Carrier Localization in InAs/InAsSb T2SLs

The experimental evidence in Section 3.2 is a strong indication that carrier localization exists in group B samples [36][40], but does not exist in group A or group C samples. As described in Section 3.1, the origin of the localization is the random disorder in the materials which generates potential fluctuations, and leads to local potential minima, acting as localization centers in the semiconductor [40]. The carrier

localization observed in this study can be due to bulk material properties, or associated with superlattices structures. The layer thickness and Sb alloy composition fluctuations can generate localization centers and these fluctuations can happen laterally within one layer or vertically from layer to layer [49][56]. For example, Figure 3.10 (a) schematically shows the carrier localization due to layer-to-layer thickness fluctuations. The thicker layers generate lower energy states which are decoupled from the miniband, and thus become localized states. The case of the carrier localization due to the intra-layer disorder along the lateral direction is shown in Figure 3.10 (b). The epitaxially grown material usually forms island-like interfaces, therefore, the layer thickness has a fluctuation of one monolayer. As a result, the thicker part generates energy states lower than average, and these low energy states become localized states.

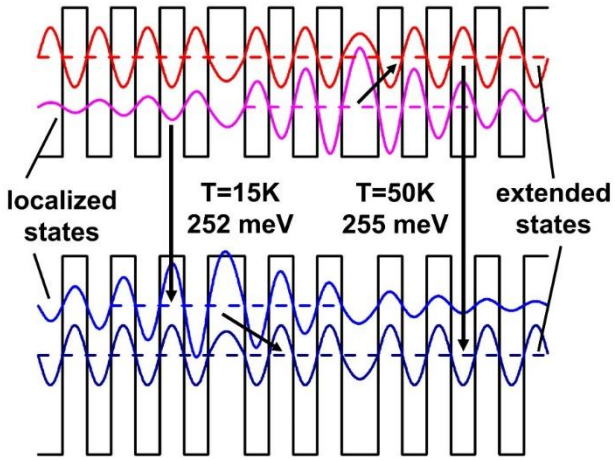

(a)

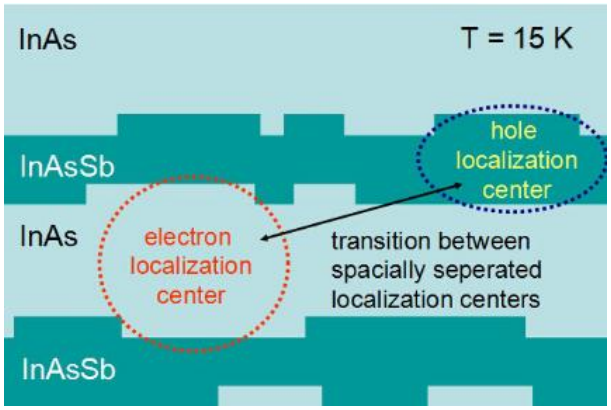

(b)

Figure 3.10. Schematic representation of the carrier localization due to layer-to-layer thickness fluctuation along (a) the vertical direction and (b) the lateral direction. The localized states are generated when one layer is thicker than the surrounding layers in the superlattice. The values are based on the experimental observations of B1875.

Since sample A (bulk InAsSb) does not exhibit any PL peak blue shift or linewidth broadening, the possibility of disorder in the bulk material, such as dopant atoms acting as localization centers, can be excluded. Therefore, the localization is related to the period of the superlattice or the Sb composition of the InAsSb layer. Since group C (long period samples) contains a larger Sb mole fraction than some of the group B (short period samples) in the InAsSb layers, the absence of carrier localization in sample C indicates that Sb composition fluctuation in the InAsSb layers is not the main causes of carrier localization. Therefore, the strong carrier localization in sample B is most probably due to the superlattice periods. Two types of disorders related with the period can take place. First, Sb diffusion from InAsSb layers to InAs layers [57][58]

can lead to a graded interface between InAs and InAsSb layers in the superlattices instead of an abrupt one. Calculation shows that this situation can change the miniband edge as large as 10 meV. However, it is difficult to estimate the effect of the fluctuation of such intermixing across the sample due to lack of quantitative experimental data. Another type of disorder is the layer thickness fluctuations on the order of one monolayer are expected in MBE-grown samples [56], which can be evaluated more quantitatively. Such layer thickness fluctuations are similar in sample B and sample C due to their similar lattice constants. The InAs and InAsSb thicknesses in sample B are smaller than those in sample C, therefore a monolayer variation in thickness is a greater fraction of the total layer thickness of sample B than that of sample C, leading to a stronger potential fluctuation.

Numerical calculation is utilized to quantitatively compare the degree of disorder in samples B and C due to thickness fluctuation. A strict calculation must contain a stochastic model to account for the random distribution of the layer thicknesses. A simplified model is acceptable based on the following considerations. First, when layer-to-layer thickness fluctuation (Figure 3.10 (a)) is dominant, a transfer matrix method can be used to calculate the energy states when one layer deviates from the periodicity. The results show that the energy of the localized state for either electrons or holes are mainly determined by the single quantum well whose width deviates from the periodicity, and the wave function will be localized in that abnormal quantum well.

The energy shift in the case of a single quantum well differs by less than 10 % compared with that of a superlattice. Second, when intra-layer thickness fluctuations (Figure 3.10 (b)) dominates, considering the fact that the island size of the InAs and InAsSb layers during growth is (30~50) nm, and the Bohr radius of the excitons in InAs and InAsSb is ~ 80 nm, the energy of the localized state can be influenced by a couple of islands in the lateral direction. The wave function is localized in the wider well, based on the estimation using perturbation theory, the energy shifts can be influenced by the neighboring islands for less than 50 %.

Under such considerations, the layer-to-layer thickness variation model can account for more than 50 % of the energy difference between the extended states and the localized states, therefore, it is reasonable to be used as an approximation. A transfer matrix method, which assumed one layer deviates from superlattice periodicity, is utilized to calculate and compare the effect of such disorder in samples B and C. In InAs/InAsSb T2SLs, the electron quantization energy is mainly determined by the thickness of the InAs layer, and the hole quantization energy is mainly determined by the thickness of the InAsSb layer. The energy shift of the localized states due to the thickness variation is shown in Figure 3.11. In Figure 3.11 (a), an InAs layer thickness variation of 1 monolayer causes a 1.6 meV shift of the electron quantization energy in sample B, 167 % larger than the shift of 0.6 meV present in sample C. In Figure 3.11 (b), 1 monolayer fluctuation of the InAsSb layer thickness causes the hole quantization

energy to fluctuate 3.0 meV in sample B, 150 % larger than the shift of 1.2 meV seen in sample C. These comparisons of energy shifts indicate a weaker potential fluctuation in sample C than in sample B. Therefore, the carriers in sample C require much lower thermal energy to overcome the localization potential barrier introduced by the monolayer fluctuation. This calculation shows that a superlattice with a shorter period has a larger potential variation due to the random monolayer variation of InAs and InAsSb layer thicknesses. Note that the energy fluctuations in sample B are comparable to the average carrier kinetic energy of 1.9 meV at 15 K, therefore they can be responsible for the carrier localization in InAs/InAsSb T2SLs. As a result, PL peak blue shift and linewidth broadening at low temperature are observed only in sample B, and not in sample C. Therefore, it is confirmed that the carrier localization is due to the layer thickness fluctuation in InAs/InAsSb superlattices 0[23], similar to that previously observed in GaAs/AlGaAs quantum wells [49]. Furthermore, the effect of Sb intermixing fluctuation leads to more disorders and therefore stronger carrier localization is expected.

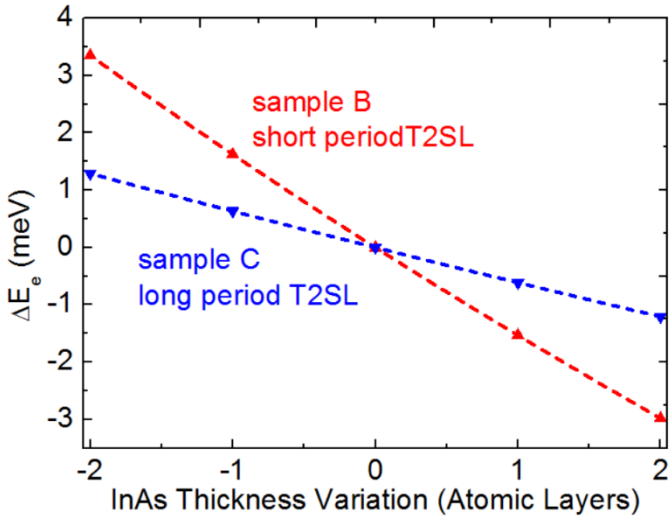

(a)

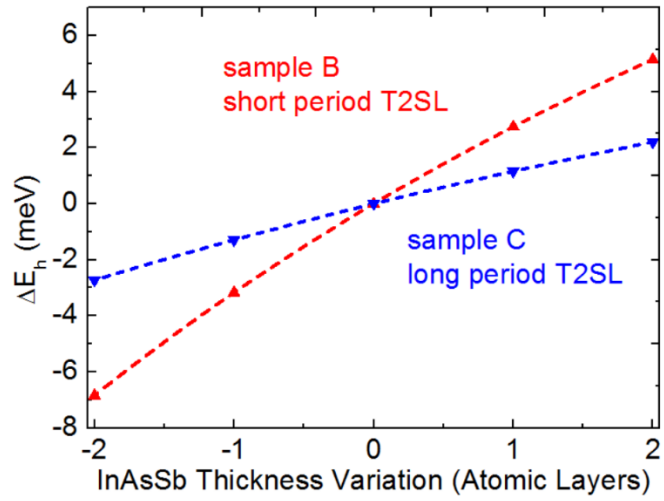

(b)

Figure 3.11. Electron and hole energy shift of the decoupled states ΔE_e and ΔE_h introduced by a disordered InAs (a) and InAsSb (b) layer in samples B and C at 15 K.

3.4. Possible Influence on Photodetectors

In InAs/InAsSb T2SLs with periods shorter than sample B (9.9 nm), the potential variation is larger and carrier localization could potentially occur at higher temperatures, such as 77 K where typical infrared photodetectors operate. In such cases, the carrier localization can influence the photodetector performance. Dark current and

carrier extraction efficiency are important parameters of a typical photodetector, the former influences the noise and the later influences the responsivity, and both can be influenced by carrier localization. On one hand, the dark current of a photodetector is typically dominated by generation-recombination (GR) current at high temperatures, and drift current at low temperature. The GR dark current is determined by the spatially direct generation process, and therefore is not affected by carrier localization. However, one cannot use the measured recombination lifetime to estimate the GR dark current, since it is much longer than the spatially direct generation lifetime. The drift current is related to the minority carrier diffusion length, which may change under carrier localization. On the other hand, the carrier extraction efficiency is also determined by the minority carrier diffusion length. The influence of carrier localization on minority carrier diffusion length is the key to understanding how carrier localization influences photodetector responsivity. The minority carrier diffusion length is related to the carrier mobility and lifetime by $\mathrm{L} = \sqrt{D\tau} = \sqrt{\frac{kT}{e}\mu\tau}$. Here D is the diffusivity, μ is mobility and τ is the carrier recombination lifetime. When carrier localization occurs, the lifetime increases but the mobility decreases. The overall effect is unknown, and the minority carrier lifetime cannot be used as a single indicator of device performance. In the next chapter, further experimental results are presented to investigate how carrier localization changes the minority carrier diffusion length.

3.5. Summary

The influence of carrier localization on carrier recombination processes in a bulk InAsSb alloy (group A), short period InAs/InAsSb T2SLs (group B) and a long period InAs/InAsSb T2SLs (group C) strain-balanced to the substrate, are evaluated using TRPL and temperature-dependent PL measurements. The minority carrier lifetimes are determined to be 1.24 μs for the bulk InAsSb alloy, and 12.8 μs for the short period InAs/InAsSb T2SL at 15 K. The PL peak energy of the short period InAs/InAsSb T2SL shows a significant blue shift of 3 meV when temperature increases from 15 K to 50 K, indicating strong carrier localization in this temperature range. The carrier localization is a result of the spatial potential fluctuation due to the random disorder of InAs and InAsSb layer thicknesses, as confirmed by numerical calculation. As a comparison, the long period InAs/InAsSb T2SL, which has larger InAs and InAsSb layer thickness, thus less spatial potential fluctuations, does not show any blue shift of the PL peak energy. Under the influence of carrier localization, the excess carriers distribute in the localized states with small electron and hole wave function overlaps, and the minority carrier lifetime below 50 K in the MWIR InAs/InAsSb T2SL is significantly enhanced.

It is desirable to have a long SRH lifetime in InAs/InAsSb T2SLs as it leads to long carrier lifetime and high mobility. However, as carrier localization occurs, a long minority carrier lifetime is not an indication of long SRH lifetime, as the lifetime is

enhanced by the small wave function overlap between localized states. Also, even carrier localization leads to long minority carrier lifetimes, the carrier mobility in InAs/InAsSb T2SLs could be reduced. Therefore, a long minority carrier lifetime may not guarantee a long minority carrier diffusion length and a good infrared detector performance. In the next chapter, the influence of carrier localization on minority carrier diffusion length, which is a very important material parameter for photodetectors, is investigated.

4. EVALUATION OF MINORITY CARRIER VERTICAL DIFFUSION LENGTH UNDER THE INFLUENCE OF CARRIER LOCALIZATION

At high temperatures and low excitation densities, a long minority carrier lifetime is often an indicator of a low SRH recombination rate, and therefore leading to a low dark current and large carrier extraction efficiency [34]. However, as shown in Chapter 3, carrier localization occurs in InAs/InAsSb T2SLs at temperatures below 50 K and significantly enhances the minority carrier lifetime. At these low temperatures the minority carrier recombination lifetime is dominated by the spatially indirect transitions between localization centers instead of directly relating with the low SRH recombination rate. The dark current and carrier extraction efficiency of the photodetectors are greatly influenced by the minority carrier diffusion length in the photodetector material. The influence of carrier localization below 50 K on the minority carrier diffusion length in InAs/InAsSb T2SL photodetectors is evaluated in this chapter.

4.1. Review of the Methods for Minority Carrier Diffusion Length Measurement

The minority carrier diffusion length is determined by $\mathrm{L} = \sqrt{D\tau} = \sqrt{\frac{kT}{e}\mu\tau}$, where D is the diffusivity, μ is the minority carrier mobility and τ is the minority carrier lifetime. The minority carrier lifetime can be measured using TRPL, so the minority carrier mobility and diffusion length are correlated. Available methods of characterizing the vertical carrier mobility or diffusion length are discussed in this section.

The Hall measurement is a commonly used method to measure the lateral carrier

mobility in a magnetic field. However, in highly anisotropic materials, such as InAs/InAsSb T2SLs, the carrier transport is very different along different directions. Along lateral directions, the carriers transport in the same layer of the superlattice, along the vertical direction, the carriers go through multiple interfaces between InAs and InAsSb with different scattering mechanisms. It is very common to extract current from the vertical direction in quasi-one-dimensional photodetectors, in which case the carrier transport along the vertical direction determines the overall carrier extraction efficiency and the diffusion current. On the other hand, the lateral mobility mainly influences the distribution of the current. It is therefore important to investigate the vertical transport which is not easily measured by Hall measurement.

A method of measuring the vertical carrier transport is the time-of-flight (ToF) experiment. This experiment can be done both electrically [59][60][61][62] and optically [62][63][64][65]. When the luminescence decay is dominated by carrier transport instead of recombination, the TRPL signal can be used for carrier transport characterization [62]. In the all-optical approach, a narrower band gap material is placed underneath the material of interest as an optical marker, and they have a type-I band edge alignment, ensuring that the excess carriers excited in the material of interest can move into to the bottom semiconductor. This type of structures has been used for optical characterizations of wide band gap materials [63][64], and more recently has been used for narrow band gap materials [65]. An ultra-short pulse laser with a pulse width on the

order of pico-seconds, incidents on the top surface of the sample, excites the excess carriers near the top surface. In an ideal case, where all the carriers are generated at the top surface, the time difference between the laser pulse and the luminescence peak from the bottom layer relates with the transient time of minority carrier transport. Practically, the luminescence peak from the bottom layer is not distinguishable from the laser pulse due to broad initial carrier distribution. The transient processes of the carriers in the device need to be modeled and fit to the experimental results to determine the carrier mobility. Instead of measuring the luminescence signal in the optical approach, the electrical ToF experiments measures the current or voltage signal from the device under a DC bias to generate an electric field to determine the field dependent vertical drift mobility. The carriers are injected using an electron beam or a laser pulse into the sample. The carrier transport information can be extracted from the delay and shape of the output pulse. For typical compound semiconductors with thickness of a few microns, the transient time during the ToF experiments is usually from a few hundred pico-seconds to a few nano-seconds.

Electron beam induced current (EBIC) can also be used to measure the minority carrier diffusion length 0[66]. An electron beam is moved along the desired direction, and the beam induced current is collected by the junction. To characterize the vertical transport properties of a semiconductor sample, the move of the electron beam along the vertical direction can be made by changing the electron energy with normal

incidence, or by illuminating the beam on the cross section of the sample. The minority carrier diffusion length can be determined from the relation between the output current and the beam position. This technique is used to characterize the minority carrier vertical transport in InAs/InAsSb photodetector with nBn structure [67]0.

Surface photovoltage (SPV) technique is a traditional used method to measure the diffusion length of minority carriers, taking advantage of the different absorption coefficients at different light wavelengths. Since its initial proposal in the 1950s, this contactless and fast technique has been widely used to for almost all the important material systems including group IV materials, III-V materials, II-VI materials, and other materials [66]. Different absorption coefficients lead to different initial carrier distributions and different SPV with excitations using light of different wavelengths. In the early SPV experiments the key assumption is infinite absorber thickness. The thickness of the absorber must be much longer than both the minority carrier diffusion length and the light penetration depth. These assumptions greatly simplify the mathematical equations to solve the carrier distribution. Under these assumptions the light penetration depth has a linear relationship with the reciprocal of the SPV, or the light intensity, and the carrier diffusion length is determined by its intercept on the penetration depth axis [66]0. Later studies pay more attention to thin absorber thickness, where the above assumptions are no longer valid. J. Lagowski derived a more general case of the SPV method with a finite device thickness, comparable to the minority

carrier diffusion length and the light penetration depth [68]. With the above assumptions released, a new linear relation between the SPV and the light penetration depth is established. However, to achieve such a linear relation, a very large interface recombination velocity at the bottom interface has to be assumed. Some techniques are used to improve the measurement capability, such as using back light illumination to separate the front and back interface effects [69], and using short circuit current as an indicator of constant SPV [70].

In practice, the ToF method requires equipment with high time resolution, and the EBIC measurement requires complicated sample preparation. The SPV method can be conveniently done with steady state measurement, however, some assumptions must be satisfied as previously discussed. An alternative method can overcome these restrictions and can be more directly used for actual devices. Using the experimentally measured short circuit current, or quantum efficiency (QE) spectrum of the device, instead of the SPV, this method determines the minority carrier diffusion length by taking into account all the factors of the drift-diffusion model [71][72][73], which represents the equations used in the SPV method. This chapter will focus on analyzing the External Quantum Efficiency (EQE) spectra of the InAs/InAsSb T2SL photodetectors with PIN structures, and investigate how the carrier localization influences the minority carrier diffusion lengths.

4.2. The Method of EQE Simulation

In the classical SPV method for diffusion length determination, not all the device parameters have to be considered, since two fundamental assumptions are satisfied: 1. minority carrier diffusion length is much shorter than the device thickness; 2. light penetration depth is much shorter than the device thickness. However, in photodetectors it is desired to have a minority carrier diffusion length longer than the absorber thickness to ensure a high carrier extraction efficiency, so the first assumption is not satisfied. The absorber thicknesses should be thick enough to absorb most light, but thin to reduce the manufacturing cost, so in this case the absorber thickness is not much larger than the light penetration depth and the second assumption is not satisfied. To investigate the minority carrier diffusion length in photodetectors, it is desired to use a more general model to calculate the EQE spectrum of the device.

In PIN photodetectors, the EQE spectra can be calculated using the drift-diffusion model, which includes current equations, continuity equations and Poisson's equations. For a narrow band gap material InAs/InAsSb T2SLs, the simulation shows that the Fermi energy is often above the band edges, and a non-degenerate relationship between the Fermi-level and charge density has to be considered. The boundary conditions are considered as Ohmic contacts. Typical photodetectors work under low excitation conditions where the photon-excited carrier densities are so low that the Fermi level is not significantly changed. In this case, the drift-diffusion model gives an

output current proportional to the input light intensity. With multiple excitation sources, the carrier distribution output current is a linear combination of each individual excitation source.

The EQE spectra of a photodetector with PIN structure is related to many material and device parameters. Among all the factors, the absorption coefficient and the minority carrier diffusion length are responsible for more than 90 % of the EQE simulation result. Other parameters are also included in the model, such as effective masses, intrinsic carrier concentrations, doping concentrations, shunt elements, effective density of states, and band gaps, etc., but these factors are responsible for only less than 10 % of the simulation result.

The EQE spectra are measured by an FTIR and calibrated with a standard blackbody. The absorption coefficients are measured using transmission experiments. These experiments are described in Section 4.3. The minority carrier lifetimes are measured using the TRPL system described in Chapter 2. The light reflection at different interfaces is calculated by using the refractive indexes of the materials on each side of the interface. The band gap of InAs/InAsSb can be calculated using the Kronig-Penney model, and also can be measured using PL experiments. The other material parameters, including effective masses, refractive indexes, intrinsic carrier concentrations, effective conduction and valance band density of states, etc, are estimated using a weighted average between those of InAs and InAsSb material

parameters from references [74][75]. The carrier diffusion lengths are unknown parameters, and are determined by changing them to fit the simulated EQE spectra with the experimental data.

4.3. EQE and Absorption Coefficient Spectra

Two InAs/InAsSb T2SLs photodetector samples with PIN structure, B1858 and B1863, are used in this study. As shown in Figure 4.1, they have a top n-doped InAs contact layer, an un-intentionally doped (UID) T2SL layer, and a p-doped bottom contact layer of the same T2SL material. The detailed parameters of these two samples are shown in Table 4.1. The UID layers are n-type with an effective doping concentration of 2×10^{16} cm^{-3}.

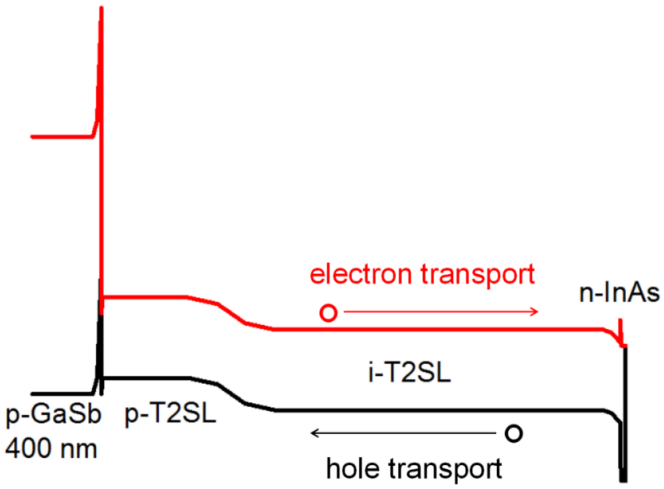

Figure 4.1. Schematic band edge alignment of the T2SL PIN photodetectors.

Table 4.1. Material and Device Parameters of Samples B1858 and B1863

		B1858	**B1863**
Superlattice parameters	**d_InAs (nm)**	4.4	5.2
	d_InAsSb (nm)	3.3	4.8
	Sb mole fraction	0.2	0.2
	Wave function overlap	0.76	0.71
Device parameters	**InAs thickness (nm)**	100	30
	InAs doping (cm^{-3})	1×10^{18}	1×10^{18}
	UID T2SL thickness (nm)	5000	2500
	UID T2SL doping (cm^{-3})	n-type, 2×10^{16}	n-type, 2×10^{16}
	Bottom contact doping (cm^{-3})	5×10^{19}	5×10^{19}

The high-resolution x-ray diffraction (XRD) results on the (004) direction of B1858 and B1863 are shown in Figure 4.2. The zeroth order superlattice peak of B1863 overlaps with the GaSb substrate peak, indicating that it is perfectly strain-balanced to the substrate, ensuring good material quality. The zeroth order superlattice peak of B1858 is different from the GaSb substrate peak, indicating that the strain in B1858 is slightly not strain-balanced.

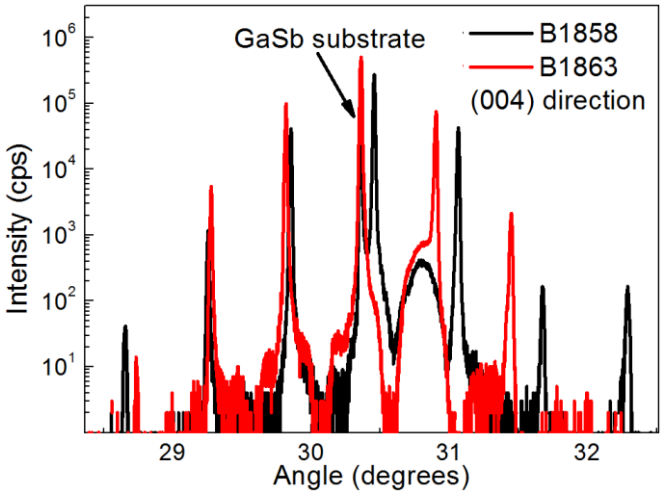

Figure 4.2. The XRD measurement results of the samples B1858 and B1863.

The EQE spectra and the absorption coefficient spectra are measured using a FTIR system. In the EQE measurement, the wire-bonded photodetector sample is placed in a cryostat with electrical output ports. The internal detector of the FTIR system is replaced with the photodetector sample. With the pre-measured spectrum of the light source and the throughput of the system, the spectral shape of the EQE is determined. A standard 800 K blackbody is then placed in front of the detector to determine the integrated responsivity in the blackbody spectral range, and later this integrated responsivity is used to calibrate the absolute value of the EQE spectra.

The EQE of both B1858 and B1863 at 15 K are shown in Figure 4.3. B1863 has a high peak EQE of 40 %, and B1858 has a low peak EQE of 16 %. For B1863, the EQE increases as photon energy increases from 230 meV to 600 meV, but for B1858, the EQE increases as photon energy increases from 250 meV to 350 meV, and then as

photon energy further increases, the EQE decreases. The notches on the curves at 290 meV, 360 meV and 470 meV are due to atmospheric absorption. Detailed analysis of the EQE spectra will be discussed along with the simulation results.

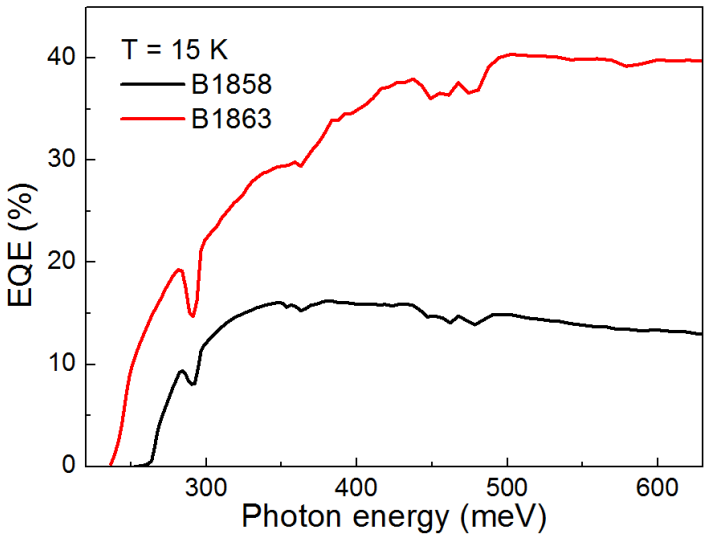

Figure 4.3. Comparison of the external quantum efficiencies of B1858 and B1863 at 15 K.

The absorption coefficients of the InAs/InAsSb T2SLs are determined from the transmission measurements by the FTIR. The T2SL on one of the two pieces are etched using a mixture of citric acid and hydrogen peroxide (citric acid : hydrogen peroxide : DI water = 1 : 1 : 1). The overall etch rates are 74 nm/min on B1858 and 84 nm/min on B1863, depending on the layer thickness and Sb composition. The etch time is controlled so that the etch depth is roughly 70 % to 90 % of the T2SL layer thickness, ensuring the largest transmission change to maximize the signal, while keeping the

GaSb buffer layer from being etched. The etch depth has a variation of 100 nm due to the etch uniformity. Comparing the spectra of the transmitted light before and after the etch yields the transmission of light in the T2SL layer which is etched away. The absorption coefficient is related to the transmitted light spectra by

$$e^{-\alpha d} = \frac{T_1}{T_0} \tag{4.1}$$

Here α is the absorption coefficient, d is the etch depth, T_1 is the spectrum of the transmitted light before etch, and T_0 is the spectrum of the transmitted light after etch. The absorption coefficient is determined by

$$\alpha = \frac{1}{d}\log\left(\frac{T_0}{T_1}\right) \tag{4.2}$$

The measured spectra of the transmitted light through sample B1858 at 15 K is shown in Figure 4.4 as an example for discussion. The black curve shows T_0 and the red curve shows T_1. The blue curve is the deducted transmission of the etched T2SL $T = T_0/T_1$. For the energy of the band gap (~270 meV) and above, T_0 and T_1 significantly differs from each other due to strong absorption of the T2SL layer. Since the GaSb substrate has absorption in the long-wavelength infrared (LWIR) region [76], the transmitted light is weak below 120 meV, introducing significant uncertainty in this range. The oscillations of the black curve between 100 meV and 270 meV demonstrate equal distance between the neighboring peaks. These oscillations are due to the interference between the multiple reflections in the T2SL layer, and do not exist above

the band gap of the T2SL (~270 meV) due to heavy absorption. The band gap energy is taken as PL peak energy minus *kT/2*. The transmission above the band gap is used to calculate the absorption coefficient using Equation 4.2 for further device simulations.

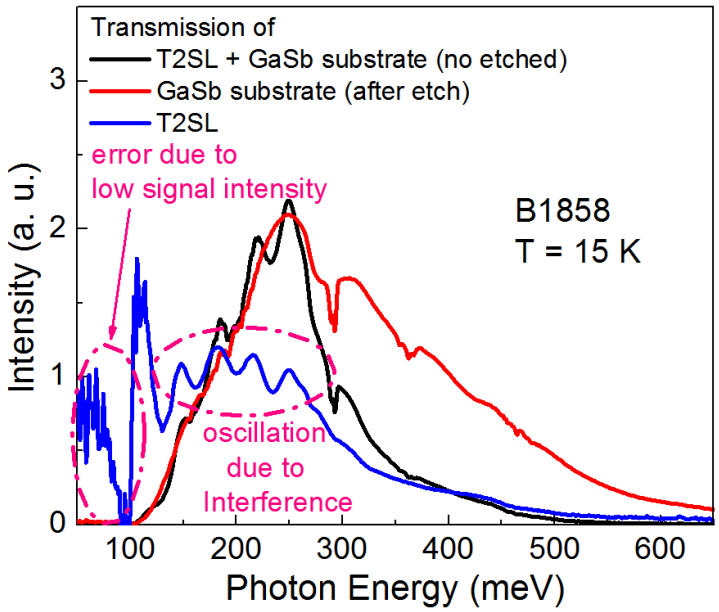

Figure 4.4. Spectra of the transmitted light of B1858 with the T2SL etched (red curve) or not etched (black curve) at 15 K. Dividing the black curve with the red curve yields the transmission of the removed T2SL layer.

The absorption coefficient of samples B1858 and B1863 at 15 K are shown in Figure 4.5. In the photon energy range between 300 meV and 430 meV, sample B1858 has a higher absorption coefficient than B1863, which is attributed to a shorter superlattice period and thus a larger wave function overlap between electrons and holes. The turning point of the absorption coefficient curve near 450 meV corresponds to the

band gap of InAs. The faster increase of the absorption coefficient in the photon energy range between 450 meV and 700 meV in B1863 can be attributed to the larger InAs/InAsSb thickness ratio leading to a stronger InAs absorption. At photon energies higher than 600 meV, the absorption of the GaSb substrate becomes strong, and both T_0 and T_1 become weaker, leading to strong noise in this range.

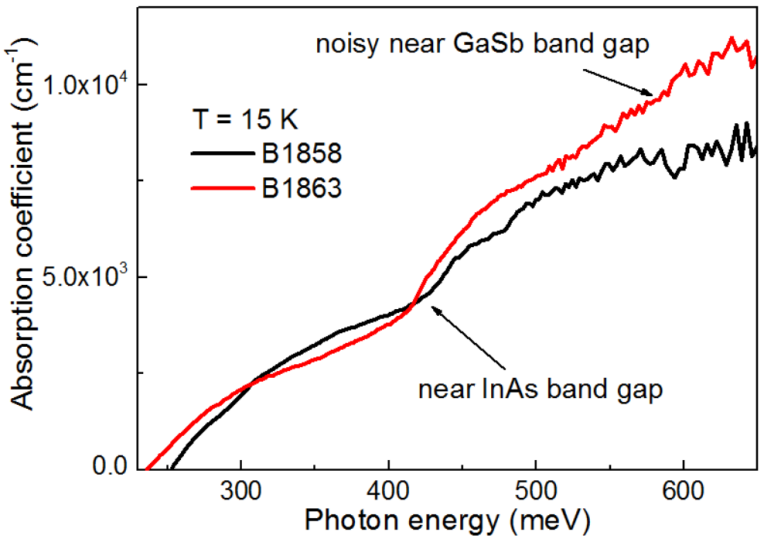

Figure 4.5. Absorption coefficients of B1858 and B1863 at 15 K.

4.4. Fitting the Model

The method described in Section 4.2 is used to simulate the EQE spectra of the T2SL PIN photodetectors. As discussed in Section 4.2, the absorption coefficient and the minority carrier (hole) diffusion length are responsible for 90 % of the EQE. Since the absorption coefficient is experimentally determined, the minority hole diffusion length dominates the simulated EQE spectra, shown in Figure 4.6 with different dot lines representing different hole diffusion lengths. Note that the absorber thicknesses

are 5 μm for B1858 and 2.5 μm for B1863. As the hole diffusion lengths become much larger than the absorber thickness, further increase of the hole diffusion length does not improve the EQE since most holes can already transport to the bottom contact and get extracted. For both samples, the saturated EQE at 2000 nm is close to 65 %, in which case most photons are absorbed and contribute to the output current. 31.5 % of the photons are reflected on the surface, and the remaining loss is due to light being transmitted into the substrate. When the hole diffusion lengths are shorter than the absorber thickness, the shape and intensity of the EQE spectra are significantly influenced. First, for the hole diffusion lengths comparable to or larger than the absorber thickness, i.e. larger than 4 μm in B1858 and 2 μm in B1863, the EQE monotonically increases with increasing photon energy. The experimentally measured EQE spectra of B1863 belongs to this situation. Second, when the hole diffusion lengths are significantly shorter than the absorber thickness, i.e. lower than 4 μm in B1858 and 2 μm in B1863, the EQE shows a peak at a certain photon energy. The experimentally measured EQE spectra of B1858 belongs to this situation. These differences are explained by the device structures as following. The intrinsic layer of the PIN photodetectors are unintentionally n-type doped, and the major contribution of the photo-current is due to the hole transport. As shown in Figure 4.1, the holes are collected in the bottom contact. With a high excitation photon energy, more light is absorbed but more carriers are generated near the top surface. If the hole diffusion

length is long enough, these photo-generated holes can be extracted effectively, and the EQE is higher. If the hole diffusion length is significantly shorter than the absorber thickness, most carriers recombine before reaching the bottom contact, and thus leads to a reduced EQE in the high photon energy region.

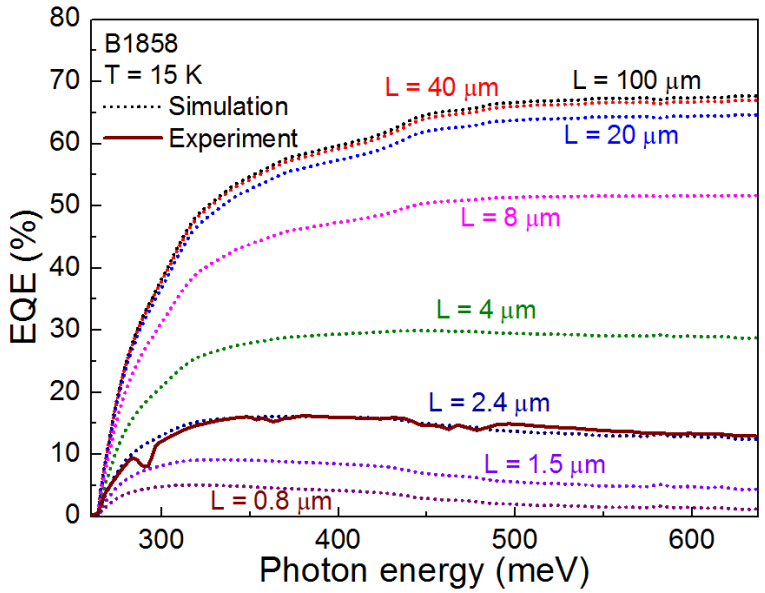

(a)

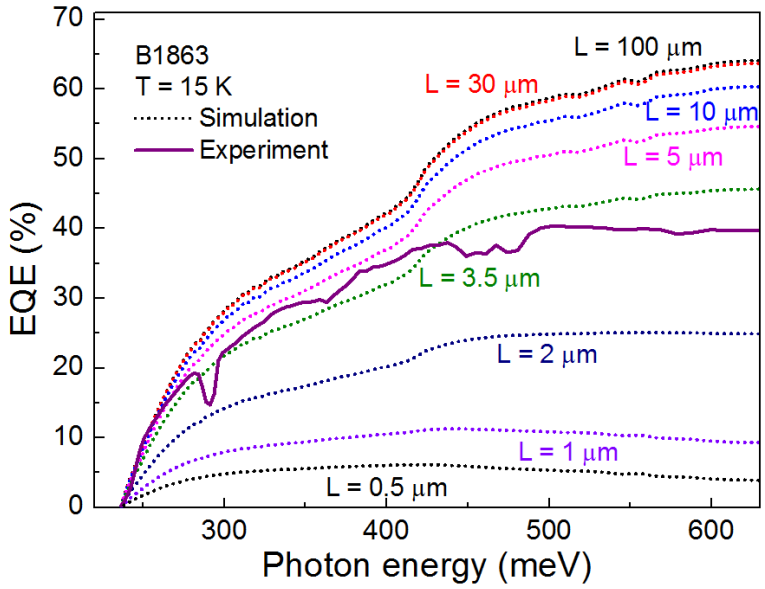

(b)

Figure 4.6. Simulated EQE with different hole diffusion length *L* (dot lines) compared

with the experimental EQE (solid lines) of (a) B1858 and (b) B1863.

The measured EQE of B1858 decreases at photon energies larger than 350 meV implies that the hole diffusion length is significantly shorter than the absorber thickness. This argument is supported by the fact that even though B1858 has a similar absorption coefficient and larger absorber thickness of 5 μm compared to 2.5 μm of B1863, the EQE of B1858 is still lower than that of B1863. Indeed, the short hole diffusion length and thick absorber layer hinders the hole transport and reduces the EQE. Therefore, for PIN photodetectors with n-type unintentionally doped absorber, a better carrier extraction efficiency can be achieved by making the p-type contact on the top and n-type contact on the bottom.

Different hole diffusion lengths are used and achieve different simulated EQE spectra to fit the experimental data. Best fits between the simulation and experiment are found to be $L = (2.4 \pm 0.8)\ \mu m$ on B1858, and $L = (3.5 \pm 1.3)\ \mu m$ on B1863 at 15 K. The error bars are based on the uncertainty of the fitting, of the absorption coefficient, and ignoring the higher order factors that account for less than 10 % of the simulation result.

Even though the high order factors are responsible for only less than 10 % of the result, some of them are worth being discussed below. First, the upper limit of the contact resistance of the devices are 50 Ohms based on I-V measurement. Simulations

show that contact resistances below this value do not influence the calculated EQE spectra. Second, the background doping level of the unintentionally doped absorber mainly influences the radiative minority carrier lifetime. Since the excitation density in the device is low, the radiative recombination is much weaker than the SRH recombination rate and thus, the doping concentration does not have significant influence on the EQE spectra. Third, the interface recombination velocities at the contact layer/absorber interfaces are estimated to be lower than 10^3 *cm/s* from the minority carrier lifetime measurement results. Simulations show that such low interface recombination velocities have limited influence on the EQE spectra.

4.5. Identification of Carrier Localization

The PL peak energy and full-width of half max (FWHM) are shown in Figure 4.7, with a low excitation density of 0.5 W/m^2. For B1863, the PL peak energy monotonically decreases as temperature increases, which is expected as the band gap energy shrinks with increasing temperature. The PL FWHM of B1863 increases monotonically as temperature increases, resulting from the flatter Fermi tail on the high energy side of the PL spectra. On the other hand, for B1858, in the temperature range from 15 K to 40 K, the PL peak energy increases with increasing temperature, the total blue shift is 2.5 meV, and the FWHM decreases as temperature increases in this temperature range.

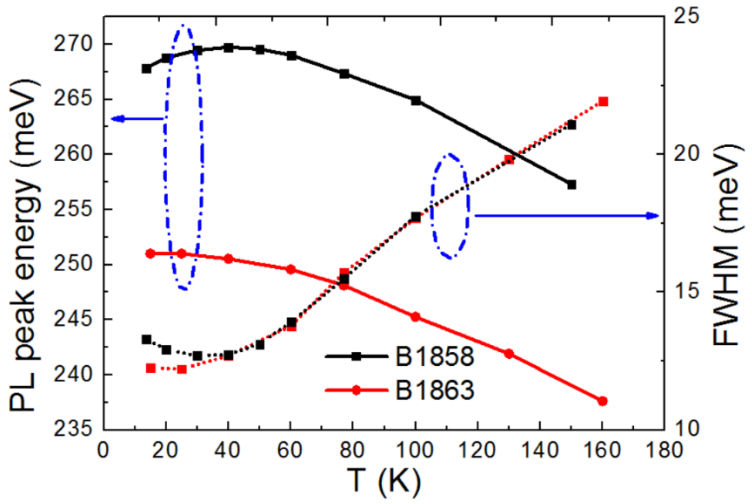

Figure 4.7. Temperature dependent PL peak energy and FWHM of samples B1858 and B1863. The solid lines represent PL peak energy, and the dot lines represent the FWHM.

The minority carrier lifetimes as a function of temperature are measured with TRPL and plotted in Figure 4.8. For B1863, when temperature increases from 15 K to 77 K, the minority carrier lifetime monotonically increases, due to the increases of radiative recombination lifetime [20]. While for the B1858, as temperature increases, the minority carrier lifetime monotonically decreases. At a temperature of 15 K, the minority carrier lifetime of 1858 is 1.65 μs, much longer than 0.70 μs at 40 K, and 0.26 μs of the B1863 at 15 K.

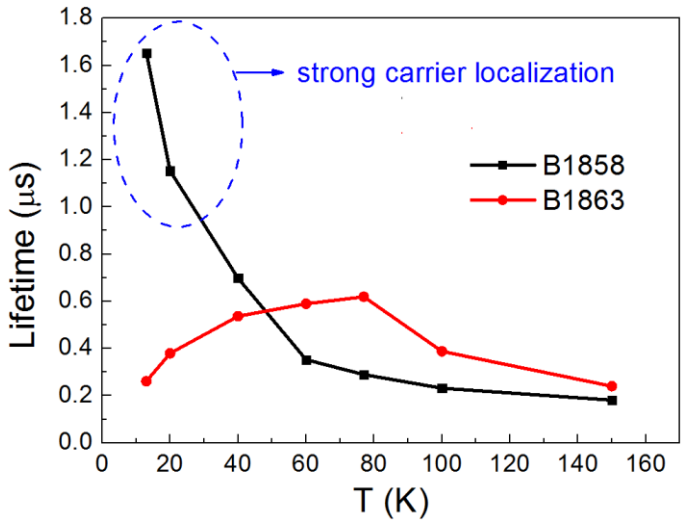

Figure 4.8. Temperature dependent minority carrier lifetimes of samples B1858 and B1863.

Based on the analysis of chapter 3, these experimental results indicate the existence of strong carrier localization in B1858 below 40 K, and carrier localization does not exist in B1863 above 15 K. The difference between these two samples are possibly due to the following two reasons. First, the period thickness of B1858 is thinner compared with that of B1863. As discussed in chapter 3, the same magnitude of layer thickness fluctuation can lead to more potential variation, and therefore carrier localization is easier to occur. Second, the XRD result in Figure 4.2 shows that the T2SL of B1858 is not perfectly strain-balanced to the GaSb substrate. This can potentially lead to more disorders such as defects, and carrier localization is more likely to occur. This point is also supported by the TRPL result at 77 K, where carrier localization does not exist in both samples. At 77 K, the minority carrier lifetime of both samples are

dominated by SRH recombination as confirmed by excitation dependent PL experiments described in [77]0. The minority carrier lifetime in B1858 is much shorter than that of B1863, indicating the SRH recombination rate is larger, possibly due to more defects.

It is worth noting that B1863 has similar T2SL period thicknesses and Sb mole fractions as those of B1875 in chapter 3. Since layer thickness fluctuation is the main origin of the carrier localization, they are expected to demonstrate a similar degree of carrier localization. However, at 15 K, B1875 demonstrates carrier localization behavior but B1863 does not. This difference is attributed to the PIN layer structure of B1863, which generates built-in electric fields.

4.6. Correlation between Carrier Localization and Hole Diffusion Length

The fitting for minority hole diffusion length described in Section 4.5 is used to extract the minority hole diffusion lengths as a function of temperature, and the results are shown in Figure 4.9. The minority hole diffusion length of these two samples demonstrate similar temperature dependence in the temperature range from 15 K to 200 K. Below 77 K, the hole diffusion lengths of both samples are nearly independent of temperatures. Indeed, the measured EQE spectra and absorption coefficient are nearly independent of temperature in this temperature range. Since the EQE spectra are mainly determined by the absorption coefficients and the minority hole diffusion lengths, the fitted minority hole diffusion length are expected to be independent of temperature

based on these experimental results. The key observations at 15 K and 77 K are summarized in Table 4.2.

Table 4.2. Key Observations from the Experiments and Simulations in Chapter 4

	Carrier localization	**Diffusion length (μm)**
B1858 at 15 K	Yes	2.4 ± 0.8
B1858 at 77 K	No	2.3 ± 0.8
B1863 at 15 K	No	3.5 ± 1.3
B1863 at 77 K	No	3.5 ± 1.4

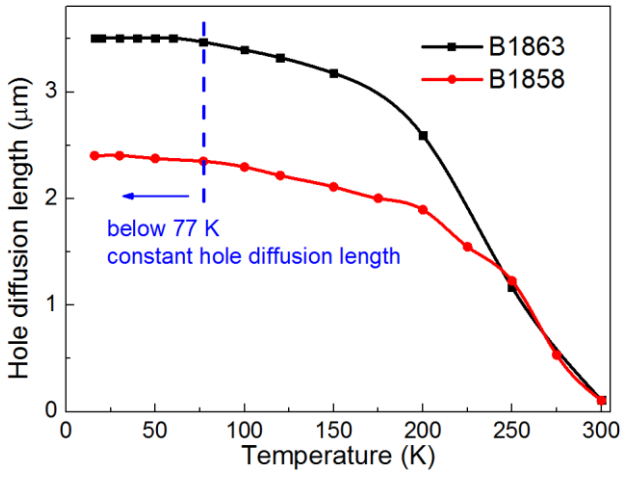

Figure 4.9. Temperature dependent hole diffusion length of samples B1858 and B1863.

The minority carrier diffusion length is determined by $L = \sqrt{D\tau} = \sqrt{\frac{kT}{e}\mu\tau}$, where D is the diffusivity, μ is the minority hole mobility and τ is the minority carrier

lifetime. In B1863, the minority hole diffusion length is independent of temperature below 77 K, indicates that $\mu\tau T$ is a constant in this temperature range. As temperature decreases, both T and τ decrease, therefore the hole mobility increases. For B1858, carrier localization occurs below 40 K, and the hole diffusion length has a similar temperature dependence with B1863 in this temperature range. As temperature decreases, the minority carrier lifetime τ increases. Compared with B1863, the increasing trend of minority hole mobility μ is reduced, but the product $\mu\tau$ has the same temperature dependence, indicating that the existence of carrier localization does not influence the minority hole diffusion length when the carrier localization is related with layer thickness fluctuation or interface roughness.

The fact that carrier localization does not influence minority hole diffusion length may be related with the wave function overlap between localized states in InAs/InAsSb T2SLs. When carrier localization occurs, the carriers can only transport via hopping process 0[41][78]. This process is related with the wave function overlap between localized states [41] and expected to have weak temperature dependence [79], as described by Mott's $T^{-1/4}$ law [43]. The "resistivity" of the hopping process is exponentially related with the distance and energy barrier between the localization centers in this phonon-assisted process [80]. The mobility μ is positively related to the wave function overlap between the hole localized states. The minority carrier lifetime τ is inversely proportional to the transition probability, thus the wave function overlap

between electron and hole localized states. Statistically these two wave function overlaps are proportional to each other. The effect of enhanced minority carrier lifetime and the reduced hole mobility may compensate each other under carrier localization, and leave the hole diffusion length un-influenced.

Since the minority carrier diffusion length is not influenced by carrier localization, the steady state parameters of InAs/InAsSb T2SL PIN photodetector, such as responsivity and detectivity are not influenced. However, based on the device parameters, the RC time constants of B1858 and B1863 are estimated to be shorter than 10 ns, while the minority carrier lifetimes are longer than 200 ns, and therefore can dominate the transient behavior of the devices. The carrier localization can enhance the minority carrier lifetimes which leads to a slower response of the device. On the other hand, since carrier localization originates from the disorder of the system, if they are due to the defect related localization centers, the non-radiative recombination rate of the material can degrade the device performance.

4.7. Summary

The drift-diffusion model is used to simulate the EQE spectra of two T2SL photodetectors with PIN structures using the experimentally measured absorption coefficients. The simulation results are compared with the experimentally measured EQE spectra to determine the minority hole diffusion lengths at different temperatures. At 15 K, the hole diffusion length in the unintentionally n-type doped regions are, *(2.4*

$\pm$ *0.8)* μm on B1858, and *(3.5* $\pm$ *1.3)* μm on B1863. The hole diffusion lengths in both samples are independent of temperature below 77 K. Carrier localization is strong in B1858 below 40 K, and weak in B1863. By comparing these two samples, it shows that the carrier localization does not influence the minority carrier diffusion length in InAs/InAsSb T2SLs, even though the minority carrier lifetime is enhanced. The steady state performance of the InAs/InAsSb T2SL photodetectors are not influenced.

5. CONCLUSIONS

This thesis develops a novel method for minority carrier lifetime measurement, and performs a comprehensive investigation of the minority carrier lifetimes and their correlation with minority carrier transport in photodetectors in InAs/InAsSb type-II superlattices (T2SLs) at temperatures below 77 K. The novel method referred to as real-time baseline correction (RBC) method significantly improves the signal-to-noise ratio of a boxcar-based time-resolved photoluminescence (TRPL) measurement systems. This method successfully measures the minority carrier lifetimes that was undetectable, leading to the discovery of long carrier lifetimes up to 12.8 μs which are the result of strong carrier localization below 50 K in the short period T2SLs. Even though the minority carrier lifetimes are enhanced by carrier localization, the minority hole diffusion lengths and responsivity in the photodetectors are not influenced.

The key of RBC method is to change the impulse response function, so as to make the system less sensitive to the dominant low frequency noise including sub-hertz baseline fluctuation and 1/f noise. The widely-used “active baseline subtraction” method cannot subtract the baseline correctly because the baseline is related to the laser pulse frequency. Another conventional method overcomes the baseline subtraction issue but is incapable of suppressing the low frequency noise. The RBC method introduces an optical chopper which divides the laser into multiple “on” and “off” states with a frequency much lower than the laser pulse frequency, and a lock-in amplifier is

introduced to measure the difference between the signal and the baseline in real-time. Equivalently, in the frequency domain, a notch filter at the modulation frequency is placed to change the impulse response, suppressing low frequency noise. The noise suppression capability of the RBC method is confirmed by the simulation, and experimental results demonstrate a signal-to-noise ratio improvement of 100 times.

A record long minority carrier lifetime of 12.8 μs at 15 K is discovered, and relate to carrier localization in the InAs/InAsSb T2SLs with short periods. In these short period T2SLs, as temperature increases, the PL peak energy demonstrates a significant blue shift as temperature increases from 15 K to 50 K. At 15 K, the high energy sides of the PL spectra deviate from Fermi distributions at low excitation densities. The long minority carrier lifetimes at 15 K decrease rapidly as temperature increases. These experimental results are strong indication of carrier localization, and their physical picture is described as following. When carrier localization occurs, the optical transition between the spatially separated localized states dominates during the PL experiment, leading to the long minority carrier lifetime, and the minority carriers do not follow a global Fermi distribution. As temperature increases the transition between the extended states become dominant, leading to the PL peak blue shift and the rapid decrease of lifetime. Comparison among the bulk InAsSb, the short and the long period InAs/InAsSb T2SLs indicates that the carrier localization originates from the atomic layer thickness fluctuation. A calculation using transfer matrix method shows that due

to the existence of atomic layer thickness fluctuation, the localization energy is 2 to 3 times larger in the short period T2SLs than in the long period T2SLs. In addition, the localization energy is close to the kT value at 15 K, confirming that the atomic layer thickness fluctuation leads to the carrier localization.

Minority carrier diffusion length is the key to understand the InAs/InAsSb T2SL photodetector operation. The external quantum efficiency (EQE) of the photodetector is dominantly determined by the absorption coefficient and the minority carrier diffusion length. Therefore, the minority carrier (hole) diffusion lengths can be determined by simulating the EQE spectra using the drift-diffusion model, with the experimentally measured absorption coefficients. A comparative study between samples that demonstrate strong or weak carrier localization indicates that when carrier localization occurs, even though the minority carrier lifetimes in the InAs/InAsSb T2SLs are enhanced, the reduced carrier transport leads to an uninfluenced minority hole diffusion length. Correspondingly, the experimentally measured responsivity of the photodetectors are unchanged, therefore, long minority carrier lifetime does not always imply improved photodetector performance.

REFERENCES

[1]. A. Rogalski, "HgCdTe infrared detector materials: history, status and outlook," *Reports on Progress in Physics*, vol. 68, p. 2267, 2005.

[2]. D. R. Rhiger, "Performance comparison of long-wavelength infrared type-II superlattice devices with HgCdTe," *Journal of Electronic Materials*, vol. 40, p. 1815, 2011.

[3]. M. A. Kinch, "Fundamentals of Infrared Detector Materials," *SPIE press, tutorial texts in optical engineering*, vol. TT76, 2007.

[4]. R. M. Biefeld, K. C. Baucom and S. R. Kurtz, "The growth of $InAs_{1-x}Sb_x$/InAs strained-layer superlattices by metalorganic chemical vapor deposition," *Journal of Crystal Growth*, vol. 137, p. 231, 1994.

[5]. Y.-H. Zhang, R. H. Miles and D. H. Chow, "InAs-$InAs_xSb_{1-x}$ type-II superlattice midwave infrared lasers grown on InAs substrates," *IEEE Journal of Selected Topics in Quantum Electronics*, vol. 1, p. 749, 1995.

[6]. Y.-H. Zhang, "Continuous wave operation of InAs/$InAs_xSb_{1-x}$ midinfrared lasers," *Applied Physics Letters*, vol. 66, p. 118, 1995.

[7]. M. J. Pullin, P. J. P. Tang, S. J. Chung, C. C. Phillips, R. A. Stradling, A. G. Norman, Y. B. Li and L. Hart, "300 K light emitting devices for the 3-10 μm band from arsenic rich InAs/$InAs_{1-x}Sb_x$ strained layer superlattices," *in Narrow Gap Semiconductors 1995*, IOP publishing Ltd., Bristol, p. 8, 1995.

[8]. Y.-H. Zhang, "InAs/$InAs_xSb_{1-x}$ type-II superlattice midwave infrared lasers," *in Optoelectronic Properties of Semiconductors and Superlattices: Antimonide-Related Strained-Layer Heterostructures*, M. O. Manasreh, Ed. Gordon Breach, p. 461, 1997.

[9]. H. S. Kim, O. O. Cellek, Z.-Y. Lin, Z.-Y. He, X.-H. Zhao, S. Liu, H. Li and Y.-H. Zhang, "Long-wave infrared nBn photodetectors based on InAs/InAsSb type-II superlattices," *Applied Physics Letters*, vol. 101, p. 161114, 2012.

[10]. E. R. Youngdale, J. R. Meyer, C. A. Hoffman, F. J. Bartoll, C. H. Grein, P. M. Young, H. Ehrenreich, R. H. Miles and D. H. Chow, "Auger lifetime enhancement in InAs-$Ga_{1-x}In_xSb$ superlattices", *Applied Physics Letters*, vol. 64, p. 3160, 1994.

[11]. D. H. Chow, R. H. Miles, J. N. Schulman, D. A. Collins and T. C. McGill, “Type II superlattices for infrared detectors and devices,” *Semiconductor Science and Technology*, vol. 6, p. C47, 1991.

[12]. C. H. Grein, J. Garland and M. E. Flatte, “Strained and unstrained layer superlattices for infrared detection,” *Journal of Electronic Materials*, vol. 38, p. 1800, 2009.

[13]. G. C. Osbourn, L. R. Dawson, R. M. Biefeld, T. E. Zipperian, I. J. Fritz and B. L. Doyle, “III-V strained layer superlattices for long-wavelength detector applications: Recent progress,” *Journal of Vacuum Science and Technology A*, vol. 5, p. 3150, 1987.

[14]. Y. Huang, J.-H. Ryou, R. D. Dupuis, V. R. D'Costa, E. H. Steenbergen, J. Fan, Y.-H. Zhang, A. Petschke, M. Mandl and S.-L. Chuang, “Epitaxial growth and characterization of InAs/GaSb and InAs/InAsSb type-II superlattices on GaSb substrates by metalorganic chemical vapor deposition for long wavelength infrared photodetectors,” *Journal of Crystal Growth*, vol. 314, p. 92, 2011.

[15]. D. H. Chow, R. H. Miles, J. R. Soderstrom and T. C. McGill, “Growth and characterization of InAs/GaInSb strained-layer superlattices,” *Applied Physics Letters*, vol. 56, p. 1418, 1990.

[16]. C. H. Grein, M. E. Flatte and H. Ehrenreich, “Comparison of ideal InAs/InAsSb and InAs/InGaSb superlattice IR detectors,” *Electrochemical Society Proceedings*, vol. 95-28, p. 211, 1995.

[17]. B. C. Connelly, G. D. Metcalfe, H. Shen and M. Wraback, "Direct minority carrier lifetime measurements and recombination mechanisms in long-wave infrared type II superlattices using time-resolved photoluminescence,” *Applied Physics Letters*, vol. 97, p. 251117, 2010.

[18]. D. Donetsky, S. P. Svensson, L. E. Vorobjev and G. Belenky, “Carrier lifetime measurements in short-period InAs/GaSb strained-layer superlattices structures,” *Applied Physics Letter*, vol. 95, p. 212104, 2009.

[19]. D. Donetsky, G. Belenky, S. Svensson and S. Suchalkin, “Minority carrier lifetime in type-2 InAs-GaSb strained-layer superlattices and bulk HgCdTe materials,” *Applied Physics Letters*, vol. 97, p. 052108, 2010.

[20]. E. H. Steenbergen, B. C. Connelly, G. D. Metcalfe, H. Shen, M. Wraback, D.

Lubyshev, Y. Qiu, J. M. Fastenau, A. W. K. Liu, S. Elhamri, O. O. Cellek and Y.-H. Zhang, "Significnatly improved minority carrier lifetime observed in a long-wavelength infrared III-V type-II superlattice comprised of InAs/InAsSb," *Applied Physics Letters,* vol. 99, p. 251110, 2011.

[21]. B. V. Olson, E. A. Shaner, J. K. Kim, J. F. Klem, S. D. Hawkins, L. M. Murray, J. P. Prineas, M. E. Flatte and T. F. Boggess, "Time-resolved optical measurements of minority carrier recombination in a mid-wave infrared InAsSb alloy and InAs/InAsSb superlattice," *Applied Physics Letters*, vol. 101, p. 092109, 2012.

[22]. Y. Aytac, B. V. Olson, J. K. Kim, E. A. Shaner, S. D. Hawkins, J. F. Klem, M. E. Flatte and T. F. Boggess, "Effects of layer thickness and alloy composition on carrier lifetimes in mid-wave infrared InAs/InAsSb superlattices," *Applied Physics Letters*, vol. 105, p. 022107, 2014.

[23]. Z.-Y. Lin, S. Liu, E. H. Steenbergen and Y.-H. Zhang, "Influence of carrier localization on minority carrier lifetime in InAs/InAsSb type-II superlattices," *Applied Physics Letters,* vol. 107, p. 201107, 2015.

[24]. B. C. Connelly, G. D. Metcalfe, H. Shen, M. Wraback, C. L. Canedy, I. Vurgaftman, J. S. Melinger, C. A. Affouda, E. M. Jackson, J. A. Nolde, J. R. Meyer and E. H. Aifer, "Investigation of trap states in mid-wavelength infrared type II superlattices using time-resolved photoluminescence," *Journal of Electronic Materials*, vol. 42, p. 3203, 2013.

[25]. A. D. Prins, M. K. Lewis, Z. L. Bushell, S. J. Sweeney, S. Liu and Y.-H. Zhang, "Evidence for a defect level above the conduction band edge of InAs/InAsSb type-II superlattices for applications in efficient infrared photodetectors," *Applied Physics Letters*, vol. 106, p. 171111, 2015.

[26]. L. Hoglund, D. Z. Ting, A. Khoshakhlagh, A. Soibel, C. J. Hill, A. Fisher, S. Keo and S. D. Gunapala, "Influence of radiative and non-radiative recombination on the minority carrier lifetime in midwave infrared InAs/InAsSb superlattices," *Applied Physics Letters*, vol. 103, p. 221908, 2013.

[27]. L. Hoglund, D. Z. Ting, A. Soibel, A. Fisher, A. Khoshakhlagh, C. J. Hill, L. Baker, S. Keo, J. Mumolo and S. D. Gunapala, "Influence of carrier concentration on the minority carrier lifetime in mid-wavelength infrared InAs/InAsSb superlattices," *Infrared Physics and Technology*, vol. 70, p. 62, 2015.

[28]. Y. Lin, D. Wang, D. Donetsky, G. Belenky, H. Hier, W. L. Sarney and S. P.

Sevensson, “Minority carrier lifetime in Beryllium-doped InAs/InAsSb strained layer superlattices,” *Journal of Electronic Materials*, vol. 43, p. 3184, 2014.

[29]. Signal Recovery Technical Notes TN 1005, “What is a boxcar averager?” last access 09/26/2016, available: http://123.physics.ucdavis.edu/week_1_files/Boxcar_Averager.pdf

[30]. P. A. Lawless and G. E. Spangler, “Baseline corrector for boxcar integrator instruments and its application to plasma chromatography,” *Review of Scientific Instruments*, vol. 48, p. 240, 1976.

[31]. A. R. Reisinger, R. N. Roberts, S. R. Chinn and T. H. Myers II, “Photoluminescence of infrared sensing materials using an FTIR spectrometer,” *Review of Scientific Instrumentation*, vol. 79, p. 82, 1989.

[32]. T. H. Wilmshurst, *Signal recovery from noise in electronic instrumentation*, Bristol-Boston: Adam Hilger Ltd., 1985.

[33]. E. H. Steenbergen, B. C. Connely, G. D. Metcalfe, H. Shen, M. Wraback, D. Lubyshev, Y. Qiu, J. M. Fastenau, A. W. K. Liu, S. Elhamri, O. O. Cellek and Y. -H. Zhang, “Temperature-dependent minority carrier lifetimes of InAs/InAsSb type-II superlattices,” *Proceeding of SPIE*, vol. 8512, p. 85120L-1, 2012.

[34]. V. Gopal, E. Plis, J.-B. Rodriguez, C. E. Jones, L. Faraone and S. Krishna, “Modeling of electrical characteristics of midwave type II InAs/GaSb strain layer superlattice diodes,” *Journal of Applied Physics*, vol. 104, p. 124506, 2008.

[35]. L. Hoglund, D. Z. Ting, A. Khoshakhlagh, A. Soibel, C. J. Hill, A. Fisher, S. Keo and S. D. Gunapala, “Influence of radiative and non-radiative recombination on the minority carrier lifetime in midwave infrared InAs/InAsSb superlattices,” *Applied Physics Letters*, vol. 103, p. 221908, 2013.

[36]. Y.-H. Cho, G. H. Gainer, A. J. Fischer, J. J. Song, S. Keller, U. K. Mishra and S. P. DenBaars, “’S-shaped’ temperature-dependent emission shift and carrier dynamics in InGaN/GaN multiple quantum wells,” *Applied Physics Letters*, vol. 73, p. 1370, 1998.

[37]. M. Kondow, S. Minagawa, Y. Inoue, T. Nishino and Y. Hamakawa, “Anomalous temperature dependence of the ordered $Ga_{0.5}In_{0.5}P$ photoluminescence spectrum,” *Applied Physics Letters*, vol. 54, p. 1760, 1989.

[38]. S. M. Olsthoorn, F. A. J. M. Driessen, A. P. A. M. Eijkelenboom and L. J. Giling, "Photoluminescence and photoluminescence excitation spectroscopy of $Al_{0.48}In_{0.52}As$," *Journal of Applied Physics*, vol. 73, p. 7798, 1993.

[39]. A. Chomette, B. Deveaud and A. Regreny, "Observation of carrier localization in intentionally disordered GaAs/GaAlAs superlattices," *Physics Review Letters*, vol. 57, p. 1464, 1986.

[40]. T. Nuytten, M. Hayne, B. Bansal, H. Y. Liu, M. Hopkinson and V. V. Moshchalkov, "Charge separation and temperature-induced carrier migration in $Ga_{1-x}In_xN_yAs_{1-y}$ multiple quantum wells," *Physics Review B*, vol. 84, p. 045302, 2011.

[41]. B. Kramer and A. MacKinnon, "Localization: theory and experiment," *Reports on Progress in Physics*, vol. 56, p. 1469, 1993.

[42]. N. F. Mott, "Conduction in non-crystalline materials III. Localized states in a pseudogap and near extremities of conduction and valence bands," *Philosophical magazine*, vol. 19, p. 835, 1969.

[43]. N. F. Mott, E. A. Davis, *Electronic Processes in Non-Crystalline Materials*, London, Oxford University Press, 1979.

[44]. I. Shlimak, *Is Hopping a Science?: Selected Topics of Hopping Conductivity*, section 2.3, p. 28, World Scientific Publishing Co. Pte. Ltd., New Jersey, 2015.

[45]. L. Grenouillet, C. Bru-Chevallier, G. Guillot, P. Gilet, P. Duvaut, C. Vannuffel, A. Million and A. Chenevas-Paule, "Evidence of strong carrier localization below 100 K in a GaInNAs/GaAs single quantum well," *Applied Physics Letters*, vol. 76, p. 2241, 2000.

[46]. J. Mickevicius, J. Jurkevicius, G. Tamulaitis, M. S. Shur, M. Shatalov, J. Yang and R. Gaska, "Influence of carrier localization on high-carrier-density effects in AlGaN quantum wells," *Optical Express*, vol. 22, p. A491, 2014.

[47]. F. A. J. M. Driessen, G. J. Bauhuis, S. M. Olsthoorn and L. J. Giling, "Effects of confined donor states on the optical and transport properties of ordered $GaInP_2$ alloys," *Physical Review B*, vol. 48, p. 7889, 1993.

[48]. B. T. McDermott, K. G. Reid, N. A. El-Masry, S. M. Bedair, W. M. Duncan, X. Yin and F. H. Pollak, "Atomic layer epitaxy of GaInP ordered alloy," *Applied Physics Letters*, vol. 56, p. 1172, 1990.

[49]. J. Hegarty and M. D. Sturge, "Exciton localisation in quantum well structures", *Surface Science*, vol. 196, p. 555, 1988.

[50]. T. Yamamoto, M. Kasu, S. Noda and A. Sasaki, "Photoluminescent properties and optical absorption of AlAs/GaAs disordered superlattices," *Journal of Applied Physics*, vol. 68, p. 5318, 1990.

[51]. M. Kasu, T. Yamamoto, S. Noda and A. Sasaki, "Photoluminescent properties of $AlAs/Al_xGa_{1-x}As$ (x=0.5) disordered superlattices," *Japanese Journal of Applied Physics*, vol. 29, p. L1055, 1990.

[52]. S. F. Yoon, Y. B. Miao and K. Radhakrishnan, "The effects of Si doping in $In_{0.52}Al_{0.48}As$ layers grown lattice matched on InP substrates," *Journal of Applied Physics*, vol. 78, p. 1812, 1995.

[53]. E. H. Steenbergen, K. Nunna, L. Ouyang, B. Ullrich, D. L. Huffaker, D. J. Smith and Y.-H. Zhang, "Strain-balanced $InAs/InAs_{1-x}Sb_x$ type-II superlattices grown by molecular beam epitaxy on GaSb substrates," *Journal of Vacuum Science and Technology B*, vol. 30, p. 02B107, 2012.

[54]. S. Liu, H. Li, O. O. Cellek, D. Ding, X.-M. Shen, E. H. Steenbergen, Z.-Y. Lin, J. Fan, Z.-Y. He, J. Lu, S. R. Johnson, D. J. Smith and Y.-H. Zhang, "Impact of substrate temperature on the structural and optical properties of strain-balanced InAs/InAsSb type-II superlattices grown by molecular beam epitaxy," *Applied Physics Letters*, vol. 102, p. 071903, 2013.

[55]. H. Li, S. Liu, O. O. Cellek, D. Ding, X.-M. Shen, E. H. Steenbergen, J. Fan, Z.-Y. Lin, Z.-Y. He, Q. Zhang, P. T. Webster, S. R. Johnson, L. Ouyang, D.J. Smith and Y.-H. Zhang, "A calibration method for group V fluxes and impact of V/III ratio on the growth of InAs/InAsSb type-II superlattices by molecular beam epitaxy," *Journal of Crystal Growth*, vol. 378, p. 145, 2013.

[56]. C. Weisbuch, R. Dingle, A. C. Gossard and W. Wiegmann, "Optical characterization of interface disorder in $GaAs\text{-}Ga_{1-x}Al_xAs$ multi-quantum well structures," *Solid State Communications*, vol. 39, p. 709, 1981.

[57]. M. R. Wood, K. Kanedy, F. Lopez, M. Weimer, J. F. Klem, S. D. Hawkins, E. A. Shaner and J. K. Kim, "Monolayer-by-monolayer compositional analysis of InAs/InAsSb superlattices with cross-sectional STM," *Journal of Crystal Growth*, vol. 425, p. 110, 2015.

[58]. J. Lu, E. Luna, T. Aoki, E. H. Steenbergen, Y.-H. Zhang and D. J. Smith, "Evaluation of antimony segregation in InAs/$InAs_{1-x}Sb_x$ type-II superlattices grown by molecular beam epitaxy," *Journal of Applied Physics* **119**, 095702 (2016).

[59]. D. M. Chang and J. L. Moll, "Direct observation of the drift velocity as a function of the electric field in gallium arsenide," *Applied Physics Letters*, vol. 9, p. 283, 1966.

[60]. A. G. R. Evans and P. N. Robson, "Drift mobility measurements in thin epitaxial semiconductor layers using time-of-flight techniques," *Solid-State Electronics*, vol. 17, p. 805, 1974.

[61]. R. K. Ahrenkiel, D. J. Dunlavy, D. Greenberg, J. Schlupmann, H. C. Hamaker and H. F. MacMillan, "Electron mobility in p-GaAs by time of flight," *Applied Physics Letters*, vol. 51, p. 776, 1987.

[62]. H. Schneider, W. W. Ruhle, K. v. Klitzing and K. Ploog, "Electrical and optical time-of-flight experiemnts in GaAs/AlAs superlattices," *Applied Physics Letters*, vol. 54, p. 2656, 1989.

[63]. A. Chomette, B. Deveaud, J. Y. Emery, A. Regreny and B. Lambert, "Vertical transport in GaAs/$Ga_{1-x}Al_xAs$ superlattices observed by photoluminescence," *Solid State Communication*, vol. 54, p. 75, 1985.

[64]. B. Deveaud, J. Shah, T. C. Damen, B. Lambert, A. Chomette and A. Regreny, "Optical studies of perpendicular transport in semiconductor superlattices," *IEEE Journal of Quantum Electronics*, vol. 24, p. 1641, 1988.

[65]. B. V. Olson, L. M. Murray, J. P. Prineas, M. E. Flatte, J. T. Olesberg and T. F. Boggess, "All-optical measurement of vertical charge carrier transport in mid-wave infrared InAs/GaSb type-II superlattices," *Applied Physics Letters*, vol. 102, p. 202101, 2013.

[66]. D. K. Schroder, *Semiconductor material and device characterization*, John Wiley & sons, Inc., Hoboken, New Jersey, 2006.

[67]. D. Zuo, R. Liu and D. Wasserman, "Direct minority carrier transport characterization of InAs/InAsSb superlattice nBn photodetectors," *Applied Physics Letter*, vol. 106, p. 071107, 2015.

[68]. J. Lagowsk, A. M. Kontkiewioz and L. Jastrzebski, "Method for the measurement of long minority carrier diffusion lengths exceeding wafer thickness," *Applied Physics Letters*, vol. 63, p. 21, 1993.

[69]. C.-L. Chiang, R. Schwarz, D. E. Slobodin, J. Kolodzey and S. Wagner, "Measurement of the minority-carrier diffusion length in thin semiconductor films," *IEEE Transactions on Electron Devices*, vol. 33, p. 1587, 1986.

[70]. E. D. Stokes, T. L. Chu, "Diffusion lengths in solar cells from short-circuit current measurements," *Applied Physics Letters*, vol. 30, p. 425, 1977.

[71]. S. R. Kurtz, A. A. Allerman, C. H. Seager, R. M. Sieg and E. D. Jones, "Minority carrier diffusion, defects, and localization in InGaAsN, with 2 % nitrogen," *Appliled Physics Letters*, vol. 77, p. 400, 2000.

[72]. S. A. Mintairov, V. M. Andreev, V. M. Emelyanov, N. A. Kalyuzhnyy, N. K. Timoshina, M. Z. Shvarts and V. M. Lantratov, "Study of minority carrier diffusion length in photoactive layers of multijunction solar cells," *Physics of Semiconductor Devices*, vol. 44, p. 1084, 2010.

[73]. H. Mackel and A. Cuevas, "Determination of the diffusion length of solar cells from the spectral response of the open-circuit voltage," last access 09/26/2016, available http://solar.org.au/papers/03papers/Mackel.pdf

[74]. I. Vurgaftman, J. R. Meyer and L. R. Ram-Mohan, "Band parameters for III-V compound semiconductors and their alloys," *Journal of Applied Physics*, vol. 89, p. 5815, 2001.

[75]. Ioffe Physico-Technical Institute, semiconductors material parameters, last access 09/26/2016, available: http://www.ioffe.ru/SVA/NSM/Semicond/

[76]. A. Chandola, R. Pino and P. S. Dutta, "Below bandgap optical absorption in tellurium-doped GaSb," *Semiconductor Science and Technology*, vol. 20, p. 886, 2005.

[77]. Z.-Y. Lin, J. Fan, S. Liu, Y.-H. Zhang, "Photoluminescence study of carrier recombination processes in InAs/InAsSb type-II superlattices," *Proceeding of SPIE*, vol. 9451, p. 94510Q-1, 2014.

[78]. D. J. Thouless, "Electrons in disordered systems and the theory of localization,"

Physics Reports, vol. 13, p. 93, 1974.

[79]. U. Jahn, S. Dhar, R. Hey and O. Brandt, "Influence of localization on the carrier diffusion in GaAs/(Al,Ga)As and (In,Ga)(As,N)/GaAs quantum wells: A comparative study," *Physical Review B*, vol. 73, p. 125303, 2006.

[80]. R. Mansfield, "Hopping conduction in III-V compounds," *in Hopping transport in Solids*, M. Pollak and B. Shklovskii, p. 352, New York, NY, USA: Elsevier Science Pub. Co., 1991.